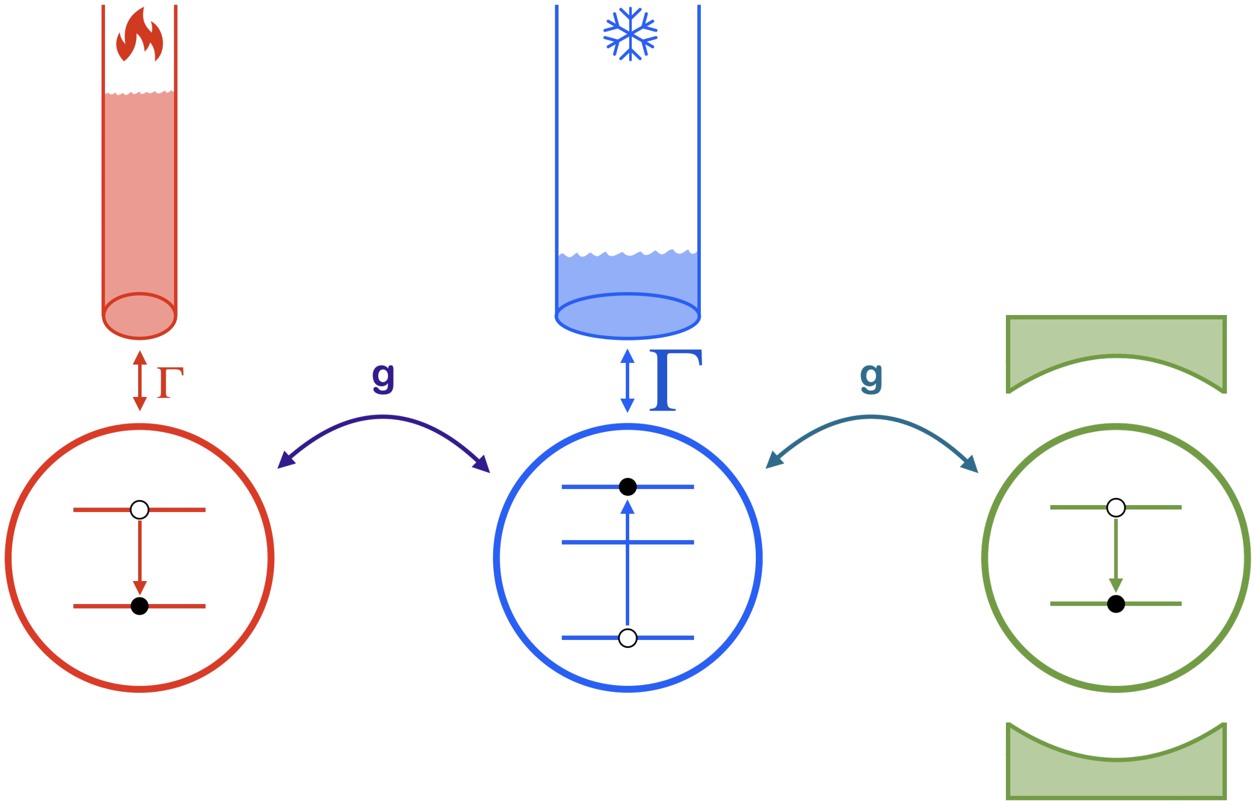

Engineering a three-atom interaction for qubit reset

Design and demonstration of an absorption refrigerator in the circuit quantum electrodynamics platform

Master Thesis in Nanotechnology

Paul Jamet Suria

Department of Microtechnology and Nanoscience
CHALMERS UNIVERSITY OF TECHNOLOGY
Gothenburg, Sweden 2022
www.chalmers.se

Master's thesis 2022

Engineering a three-atom interaction for qubit reset

Design and characterization of an absorption refrigerator in the circuit quantum electrodynamics platform

Paul Jamet Suria

Department of Microtechnology and Nanoscience (MC2)
Wallenberg Centre for Quantum Technology
202Q-lab
Chalmers University of Technology
Gothenburg, Sweden 2022

Engineering a three-atom interaction for qubit reset
Design and characterization of an absorption refrigerator in the circuit quantum electrodynamics platform
Paul Jamet Suria

Supervisor: Dr. Aamir Ali, Quantum Technology Laboratory (QT)
Examiner: Prof. Simone Gasparinetti, Quantum Technology Laboratory (QT)

Master's Thesis 2022
Department of Microtechnology and Nanoscience (MC2)
Quantum Technology Laboratory (QT)
202Q-lab
Chalmers University of Technology
SE-412 96 Gothenburg
Telephone +46 31 772 1000

Cover: Schematic diagram of the autonomous refrigeration process described in the manuscript.

Typeset in LaTeX
Printed by Chalmers Reproservice
Gothenburg, Sweden 2022

Engineering a three-atom interaction for qubit reset
Paul Jamet Suria
Department Microtechnology and Nanoscience (MC2)
Chalmers University of Technology

Abstract

Superconducting qubits cooled down to milliKelvin temperatures are regarded as a promising platform for quantum information processing. Here, a major source of errors is the poor thermalization of the qubits to their milliKelvin environments, leading to a significant residual excited-state population 1 - 13%. In this project, we have designed and experimentally characterized a proof-of-concept device aimed to reduce this residual population of a target transmon qubit and thereby reset it. Our device consists of three mutually-coupled transmon qubits including one target qubit, and two coupled waveguides. Its Hamiltonian is tailored such that an effective three-body interaction arises under a resonance condition, in which, single excitations of two qubits are coherently exchanged with a cascaded double-excitation of a third qubit. The waveguides host photons with a synthesized thermal spectral density and thus act as tunable thermal baths to the qubits. The scheme of this configuration allows to operate the device as an absorption refrigerator that is able to deplete the residual excited-state population present in the target qubit, with the net effect of cooling and resetting the qubit. In this thesis, we present the design, characterization and the evidence of the two-photon process under resonance condition in our first proof-of-concept device. We also demonstrate qubit reset allowed by the two-photon process and early evidence of autonomous reset using thermal fields. This work paves the way towards the demonstration of autonomous quantum refrigeration in the circuit quantum electrodynamics platform for qubit reset.

Keywords: Quantum Computing, Quantum Thermodynamics, Circuit Quantum Electrodynamics, Qubit Reset

Acknowledgements

This project has been conducted at Chalmers University of Technology in 202Q-lab.

I wish to express my gratitude to Prof. Simone Gasparinetti for giving me the opportunity to work in his laboratory. He has provided excellent guidance and support during the whole process and shown me the importance of taking attention to detail and being meticulous in everything you do.

My deepest thanks go to Aamir Ali for his constant help and advice. Without his help this project would have not been possible. His wide knowledge and problem solving skills allowed me to progress in a scientific and personal level. The manner in which he managed the project pushed me to give my best while enjoying the process.

I would also like to thank the rest of the 202Q-lab team for their constant advice and help during the project. It has been a pleasure working side by side with all of them and I will always remember the great moments shared around the office with all of them. I would like to particularly thank Claudia Castillo Moreno for fabricating the device measured in this thesis.

I also thank Nicole Yunger-Halpern and José Antonio Marín Guzmán for providing great insight from the theoretical point of view and for helping us understand better the physics of the device.

Paul Jamet Suria, Gothenburg, July 2022

Contents

1

Introduction

Before the discovery of Quantum Physics in the early 20th century by physicists such as Bohr, Heisenberg and Planck [1–3] many thought there was not much more to discover in Physics. This revelation inspired a revolution in many science disciplines and uncovered new problems across different platforms. Scientist had a new platform, a new lens, to look at problems in a more detailed manner. This allowed for a large number of scientific breakthroughs such as the invention of the transistor, the greatest technological revolution of mankind.

Quantum Theory was invented to understand light-matter interaction such as black-body radiation [3]. This theory allowed for a better understanding of the physics that govern the Quantum scale. The less degrees of freedom a physical system has the more 'Quantum' it behaves. In particular, reducing the dimensions of the system allows to decrease its degrees of freedom while cooling it down to cryogenic temperature allows for the system to reach it's energy ground state (GS). Under this situation quantum effects govern the behaviour of the system and with the advances of technology these systems have been experimentally measured, for instance, Serge Haroche and David Weinland received the Nobel price in 2012 for experimentally measuring and manipulation of a single quantum system. This achievement launched the second quantum revolution in which quantum system can be measured and controlled.

1.1 Superconductive circuits for quantum computing

This new ability to use quantum system prompted the question of quantum advantage. Can we use this quantum behaviour to get an advance somehow? In 1985 Richard P. Feynman theorized that the best way to simulate a quantum system such as a molecule would be to use a quantum system [4]. This idea gave birth to the concept of a quantum computer, a machine that takes advantage of quantum phenomena such as superposition and entanglement to gain an advantage over a classical computer. In essence, the calculations needed to simulate a quantum system become simpler when using a quantum machine to solve them. In 1994 Peter Shor published the first theoretical proof of quantum advantage [5], he invented an algorithm for prime number factorization that outperformed classical computers.

This advantage was achieved by using quantum properties such as superposition and interference. This discovery proved the potential in quantum computing and started the quantum computing revolution.

Having proven this advantage theoretically the challenge became to experimentally create a quantum computer capable of running this type of algorithms. A classical computer operates with bits that take values of 0 and 1, experimentally these are implemented with transistors. On the other hand, a quantum computer operates with quantum bits (qubits) which are quantum two level systems (TLS) in which a qubit can be in a superposition state of the two levels. So far different approaches of realizing a qubit have been tried including quantum dots in semiconductors, trapped ions, nitrogen-vacancy (NV) centers in diamonds and superconductive circuits.

Altought it is too early to define a standard for quantum computing at this moment one of the most widely spread and main candidate to be able to implement fault-tolerant quantum computing is superconductive circuits. In 2019 Google published the famous 'Quantum Supremacy' paper [6] in which they provided the first experimental proof of quantum advantage using superconductive circuits. Google's 53 qubit Sycamore processor was able to solve a problem exponentially faster than a classical computer simulating the same process. Governments and companies seeing the large potential in this field are fastly developing new technologies around the superconductive circuits field, for instance companies such as Bluefors and Zurich Instruments are developing cryogenic dilution refrigerators and test-and-measurement equipment in the RF/Microwave domain that support the growth of the field.

Superconductivity is a phenomena observed in metals such as aluminium at very low temperature. Below a certain critical temperature (T_c) aluminium becomes superconductive and carries current with no resistance. Under this condition electrons in the metal form a 'superfluid' made of electron pairs, named Cooper-Pairs, that do not scatter, carry no entropy and have infinite conductance. These properties allow one to create a non-dissipative system that is described by a single wavefunction and can be treated quantum mechanically. By cooling the system further the thermal fluctuations $k_B T$ become smaller than the eigenergies of the circuit elements thus allowing them to stay mostly (more detail will come in the next section) in their ground state.

1.2 Quantum computing and qubit reset

Gate-based quantum computing consists of preparing the quantum bits in their ground state as a starting point and then apply a series of transformations (gates) in order to manipulate their state to perform a calculation. At the end of the process the qubit state encodes the solution of the problem. It is then clear that preparing the initial ground state with a good fidelity is crucial for fault-tolerant computation.

Superconductive chips are placed in dilution cryostat at temperatures below 10 mK, as they thermalize with the environment they will reach their ground state, this process is called the energy relaxation of the qubit. In order to perform complex and precise calculations the relaxation time (T_1) needs to be large in order to maintain the qubit state information and not loose it to the environment. On the other hand having a large T_1 puts a constraint on the waiting time needed to reset a qubit for a new calculation. The aim of this thesis is to design and characterize the performance of a novel qubit reset scheme with an engineered two-photon process providing faster than T_1 qubit reset.

1.3 Analysis of a circuit quantum electrodynamics system decay dynamics: the master equation

Isolated quantum mechanical systems evolve under the Schrödinger equation ($\hbar = 1$)

$$\dot{\rho} = -i[H, \rho] \tag{1.1}$$

where H denotes the Hamiltonian of the system defining its energy landscape and ρ is the density matrix related to the state of the system. Equation 1.1 shows how the system evolves under the commutation of the Hamiltonian and the density matrix. The Hamiltonian embeds all the interactions of the system and therefore equation 1.1 accurately describes the evolution of the system. In reality, circuit electrodynamics (cQED) systems are not isolated as they are connected to the outside world through electronics and couple to the environment which is not modeled in the Hamiltonian. These interactions are not straightforward to model and can be simplified under the Born-Markov approximations in which the environment acts as a reservoir coupled to the system where it dissipates at rate Γ. Let's consider a system consisting of a single qubit with Hamiltonian $H = \omega_q \sigma^+ \sigma^-$ coupled to the environment with decay rate Γ. In this model the Schrödinger equation (1.1) becomes [7, 8]:

$$\dot{\rho} = -i[H, \rho] + \Gamma \left[\left(n_{\omega_q}(T) + 1 \right) \mathcal{D}[\sigma^-]\rho + n_{\omega_q}(T) \mathcal{D}[\sigma^+]\rho \right] \tag{1.2}$$

where:

- Γ : Decay rate of the qubit into its environment
- $n_\omega(T) = \frac{1}{e^{\frac{\hbar\omega}{k_B T}} - 1}$:

  Thermal occupation of the environment following a Bose-Einstein distribution where T is the temperature of the environment and k_B is the Boltzmann constant.
- $\mathcal{D}[\hat{O}]\bullet = \hat{O} \bullet \hat{O}^\dagger - \frac{1}{2}\{\hat{O}^\dagger \hat{O}, \bullet\}$: Lindblad dissipation super operator with $\{\cdot, \cdot\}$ the anticommutator.

Equation 1.2, commonly known as the master equation of the system, describes its evolution as it dissipates into the environment. In this example we have considered a negligible pure dephasing rate Γ_ϕ which would introduce an extra term $\frac{\Gamma_\phi}{2}\mathcal{D}[\sigma_z]\rho$ in equation 1.2 where σ_z is the Pauli rotation operator around the $\hat{z}$ axis.

In section 2.1.5 we will see how the master equation can be combined with input-output theory to obtain the reflection coefficient of a waveguide coupled to a qubit.

2

Theory

2.1 Circuit Quantization, cQED building blocks

This thesis is focused on the design and measurement of an Autonomous Qubit Reset system on the cQED platform. cQED provides a simple to fabricate single platform to study quantum physics and quantum information. It is therefore an ideal platform to engineer and study light-matter interactions. This section will explain in detail the fundamental building blocks of a cQED system.

2.1.1 The quantized LC oscillator

The autonomous reset scheme discussed in this thesis is based on the transmon qubit, a type of superconducting qubit. This system can be studied as an anharmonic quantized oscillator, to understand it we first need to look at a simplified model, the quantized LC oscillator. Following Devoret's derivation [9] we start from the well known LC circuit and we define its two nodes, ground and flux node ϕ as shown in Figure 2.1 below.

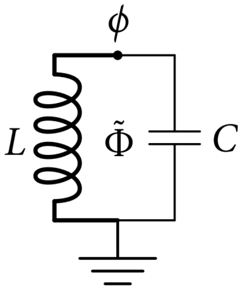

Figure 2.1: LC circuit diagram. Taken from [10]

The circuit can be studied under the classical mechanics Lagrangian formalism. The Lagrangian of the LC circuit is given by

$$\mathcal{L} = \mathcal{T} - \mathcal{V} = \frac{C\dot{\phi}^2}{2} - \frac{\phi^2}{2L} \tag{2.1}$$

Where $\mathcal{T}$ and $\mathcal{V}$ are the kinetic and potential energy terms which correspond to the energy stored in the inductor and capacitor respectively. The Hamiltonian of the system can then be retrieved from the Lagrangian by applying the Legendre transformation

$$H = \dot{\phi} q - \mathcal{L} \tag{2.2}$$

Where $q = \frac{\partial \mathcal{L}}{\partial \dot{\phi}} = C\dot{\phi}$ is the conjugate coordinate of the flux coordinate ϕ, i.e. the charge on the capacitor. The resulting Hamiltonian is a harmonic oscillator of the form:

$$H = \frac{q^2}{2C} + \frac{\phi}{2L} \tag{2.3}$$

This LC resonator has a equidistant energy levels separated by $\hbar\omega_r$ where $\omega_r = \frac{1}{\sqrt{LC}}$ is the resonator frequency. The system can be quantized by promoting the charge and flux variables to quantum-mechanical operators satisfying the commutation relation

$$[\hat{\phi}, \hat{q}] = i\hbar \tag{2.4}$$

It is convenient to express the flux and charge operators as functions of the standard creation and annihilation operators $\hat{a}^\dagger$ and $\hat{a}$

$$\hat{\phi} = \phi_{zpf} \left(\hat{a}^\dagger + \hat{a}\right) \tag{2.5}$$

$$\hat{q} = iq_{zpf} \left(\hat{a}^\dagger - \hat{a}\right) \tag{2.6}$$

Where $\phi_{zpf} = \sqrt{\hbar/2\omega_r C}$ and $q_{zpf} = \sqrt{\hbar\omega_r C/2}$ are the characteristic magnitudes of the flux and charge at the zero-point fluctuations. The Hamiltonian in equation 2.3 can now be written in the usual form as

$$H = \hbar\omega_r \left(\hat{a}^\dagger\hat{a} + 1/2\right) \tag{2.7}$$

This Hamiltonian has eigenstates $\hat{a}^\dagger\hat{a}\left|n\right\rangle = n\left|n\right\rangle$ where n defines the energy state of the oscillator and $\hat{n} = \hat{a}^\dagger\hat{a}$ is the number operator.

As discussed before, a qubit is a TLS capable of being in a superposition state. The harmonic nature of the LC oscillator does not protect against unwanted excitations of higher energy levels as they require the same energy to excite. The charge qubit addresses this problem by introducing anharmonicity in the form of a non-linear inductor, the Josephson Junction (JJ).

2.1.2 The flux-tunable transmon

The charge qubit is a modification of the LC oscillator in which the inductor has been replaced by a JJ with non-linear current characteristics

$$I = I_c \sin\left(\frac{2\pi\phi}{\Phi_0}\right) \tag{2.8}$$

where I_c is the critical current of the junction defined by its dimensions and materials and $\Phi_0 = h/2e$ is the flux quanta. The energy stored in the JJ can be calculated as

$$E = \int V(t)I(t)dt = \int \frac{d\phi}{dt} I_c \sin\left(\frac{2\pi\phi}{\Phi_0}\right) dt \tag{2.9}$$

The resulting energy stored in the JJ is then

$$E = -E_J \cos\left(\frac{2\pi\phi}{\Phi_0}\right) \tag{2.10}$$

Where we define $E_J = \Phi_0 I_c/2\pi$ as the Josephson energy associated with the coherent tunneling of Cooper pairs across the junction. By replacing the linear inductor in the LC oscillator we obtain the Hamiltonian of the capacitively shunted JJ with $\hat{\varphi} = \frac{2\pi\hat{\phi}}{\Phi_0}$(see full derivation in [11])

$$H_{SCPB} = 4E_C\left(\hat{n} - n_g\right)^2 - E_J \cos\hat{\varphi} \tag{2.11}$$

This is the general Hamiltonian of the Single Cooper Pair Box (SCPB) qubit where $E_C = e^2/2C_\Sigma$ with $C_\Sigma = C + C_{JJ}$ is the charging energy of the capacitor with C_{JJ} the junction capacitance and n_g is the offset charge accumulated on the capacitor due to an external electric field bias. The transmon is a particular case of the SCPB in which the Josephson energy is much larger than the charging energy ($E_J/E_C \gg 1$). In this configuration the charge offset becomes negligible which reduces the charge offset dependance of the energy levels at the cost of a reduced anharmonicity. Figure 2.2 shows the charge offset dependence of the first three energy levels of the SCPB Hamiltonian for different vales of E_J/E_C.

In the $E_J/E_C \gg 1$ regime the charge offset term can be neglected and the variance of the conjugate variable $\hat{\varphi}$ becomes small. Under this conditions the Hamiltonian in equation 2.11 is considered upto the fourth order of $\hat{\varphi}$

$$H_T = 4E_C\hat{n}^2 + \frac{1}{2}E_J\hat{\varphi} + \frac{1}{4}E_J\hat{\varphi}^4 \tag{2.12}$$

And we can introduce the transmon creation $\hat{b}^\dagger$ and annihilation $\hat{b}$ operators (analogous to $\hat{a}^\dagger$ and $\hat{a}$) as

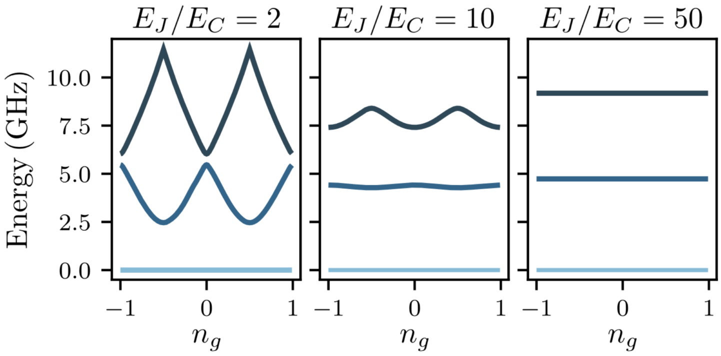

Figure 2.2: Gate charge dependence of the first three transmon levels for different regimes of E_J/E_C. Taken from [11]

$$\hat{\varphi} = \left(\frac{2E_C}{E_J}\right)^{1/4}\left(\hat{b}^\dagger + \hat{b}\right) \tag{2.13}$$
$$\hat{n} = \frac{i}{2}\left(\frac{E_J}{2E_C}\right)^{1/4}\left(\hat{b}^\dagger - \hat{b}\right)$$

The resulting Hamiltonian in the lowering and raising operators notation is given by

$$H_T = \hbar\omega_q \hat{b}^\dagger\hat{b} + \frac{\alpha}{2}\hat{b}^\dagger\hat{b}^\dagger\hat{b}\hat{b} \tag{2.14}$$

Where $\hbar\omega_q = \sqrt{8E_CE_J} - E_C$ is the first excited state energy of the transmon qubit and $\alpha = -E_C$ is the second excited state anharmonicity. For simplicity of notation we will consider $\hbar = 1$ from now on without any loss of generality. Equation 2.14 describes the transmon qubit as a three level system with anharmonicity α, the three energy eingenstates of the transmon are denoted as $|g\rangle$,$|e\rangle$ and $|f\rangle$. Their corresponding eigenenergies are 0 , ω_q and $\omega_q - \alpha$.

The eigenenergies of the transmon qubit can be rendered tunable by an external magnetic flux by replacing the JJ by a Superconductive Quantum Interference Device (SQUID). The SQUID is formed by two JJs in a superconductive ring. Applying a magnetic flux threading the ring allows to tune the frequency of the SQUID device. The E_J flux dependance is given by

$$E_J\left(\Phi_x\right) = E_{J\Sigma}\cos\left(\frac{\pi\Phi_x}{\Phi_0}\right)\sqrt{1 + d^2\tan^2\left(\frac{\pi\Phi_x}{\Phi_0}\right)} \tag{2.15}$$

Where $E_{J\Sigma}$ is the sum of the two Josephson energies of the individual junctions and $d = (E_{J2} - E_{J1})/E_{J\Sigma}$. By applying a magnetic flux on the SQUID one can tune the qubit frequency ω_q while keeping the same anharmonicity α.

The transmon qubit is often referred as an "artificial atom" as it is a discrete level system such as an atom in which the energy levels can be tailored by design. An in detail description of the design process is given in section 3.1.

2.1.3 Coplanar waveguides

The second key ingredient of the AQR system is the coplanar waveguide (CPW), as it can provide a continuum of electromagnetic modes to which the transmon can couple to. Their continuous nature also allows to host arbitrary power spectral densities (PSD) distributions. This aspect is interesting in the quantum thermodynamics field as it provides equilibrium heat baths to which a qubit can couple thus artificially modifying its eigenstate population distribution.

The coplanar waveguide is, analogous to the coaxial cable, an isolated conductive plane with inductance per unit length L_0 capacitely coupled to the ground plane. Due to its continuous nature, it cannot be modelled as a lumped element but can be described under the telegrapher model as a semi-infinite array of LC circuit sections in series as shown on the circuit in Figure 4.6b.

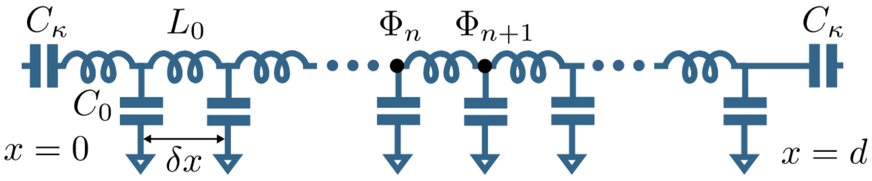

Figure 2.3: Telegrapher model of the CPW consisting of an array of LC resonators with inductance and capacitance per unit length L_0 and C_0. The C_κ capacitors indicate couplings at the end of the waveguide to other possible notes of a circuit. Taken from [11]

Under this model the Hamiltonian of the CPW will the the sum of the LC oscillator Hamiltonians as in equation 2.3 that constitute it. The sum can be expressed as an integral by taking infinitesimally short LC oscillator sections giving the Hamiltonian:

$$H_{CPW} = \int_0^d \left(\frac{1}{2C_0} \hat{q}^2(x) + \frac{1}{2L_0} (\partial_x \hat{\phi}(x))^2 \right) dx \tag{2.16}$$

As the lumped LC oscillator, this Hamiltonian can be expressed in the creation and annihilation operators as

$$H_{CPW} = \int_0^\infty \hbar\omega \left(\hat{a}_\omega^\dagger \hat{a}_\omega + 1/2 \right) d\omega \tag{2.17}$$

where $\hat{a}_\omega$ and $\hat{a}_\omega^\dagger$ are the raising and lowering operators at frequency ω satisfying $[\hat{a}_\omega, \hat{a}_\omega^\dagger] = 1$.

From equation 2.17 it is clear that the CPW has a continuum of eigenmodes for all frequencies, it can therefore host all frequency modes. This aspect of the CPW makes it an excellent artificial heat bath as one can artificially synthesize a signal of modes with any desired spectral density.

2.1.4 Qubit-Qubit coupling

Qubits can be capacitively coupled to other qubits allowing them to exchange excitations and form dressed states. The Hamiltonian of two coupled qubits is given by

$$H = \sum_{n=1}^{2} \omega_{q_i} \sigma_i^+ \sigma_i^- + g \left(\sigma_1^+ \sigma_2 + \sigma_2^+ \sigma_1 \right) \tag{2.18}$$

where we have truncated the transmon qubit to two energy levels by introducing the lowering and raising operators given by

$$\begin{aligned} \sigma^+ &= \left| g \right\rangle \left\langle e \right| \\ \sigma^- &= \left| e \right\rangle \left\langle g \right| \end{aligned} \tag{2.19}$$

and g is the coupling rate between qubit 1 and 2. Note that from this point forward the lowering and raising operator notation changes to σ^+ and σ^- instead of the previously used $b^\dagger$ and b. The Hamiltonian of the system is the sum of both qubits Hamiltonians plus an interaction term $g\left(\sigma_1^+ \sigma_2 + \sigma_2^+ \sigma_1\right)$ describing excitation exchanges between the qubits. The terms $\sigma_1^+ \sigma_2$ and $\sigma_2^+ \sigma_1$ describe the processes in which one excitation is exchanged from qubit 1 to qubit 2 and vice versa.

Under the assumption $C_g \gg C_{\Sigma_i}$, the coupling rate between two qubits is given by [12]

$$g = \frac{1}{2} \sqrt{\omega_1 \omega_2} \frac{C_g}{\sqrt{C_g + C_{\Sigma_1}} \sqrt{C_g + C_{\Sigma_2}}} \tag{2.20}$$

where ω_i denotes the frequency of each qubit, C_g is the capacitance between the two qubits and C_{Σ_i} is the total capacitance of each qubit. When two qubits are coupled together they become a single system and they get hybridized. The individual qubits bare energy states get 'dressed' and shift their frequency slightly as in the light-matter interactions in the Jaynes-Cummings model described in more detail in subsection 2.1.6.

2.1.5 Qubit-Waveguide coupling

A waveguide provides a direct path for a qubit to decay into a controllable environment. This decay can be modeled by the master equation seen in subsection 1.3.

Under this formulation the decay of the qubit can be studied using input-output theory. Starting from the master equation

$$\dot{\rho} = -i\,[H, \rho] + \Gamma\left[(n_\omega(T) + 1)\,\mathcal{D}[\sigma^-]\rho + n_(T)\mathcal{D}[\sigma^+]\rho\right] \tag{2.21}$$

The termination of the waveguide can be seen as a semi-transparent mirror in which the modes in the waveguide get reflected but also drive the qubit with a coupling rate Γ [13, 14]. Due to this 'mirror-like' nature, it is interesting to study the steady-state reflection coefficient of the waveguide when driving it with a coherent tone which is given by

$$r = \frac{\langle \alpha_{out} \rangle}{\alpha_{in}} = \frac{Tr[\rho_{ss}\alpha_{out}]}{\alpha_{in}} \tag{2.22}$$

where we used the trace formula for expectation values in a quantum system. A coherent state $|\alpha\rangle$ is an eigenstate of the creation operator $a\,|\alpha\rangle = \alpha\,|\alpha\rangle$. The steady state density matrix is obtained by solving the master equation 2.22 with the steady state condition $\dot{\rho} = 0$. This equation is not trivial and can be solved using a symbolic mathematical solver such as Mathematica. Following the derivation in [15] the resulting reflection coefficient is a Lorentzian of the form

$$r = 1 - \frac{2\Gamma_r(\Gamma_r + \Gamma_{nr} + 2i\Delta)}{\Gamma_r^2 + 2\Gamma_r\Gamma_{nr} + \Gamma_{nr}^2 + 4\Delta^2 + 2\Omega^2} \tag{2.23}$$

Where we have split the decay rate $\Gamma = \Gamma_r + \Gamma_{nr}$ into its radiative part corresponding to the qubit radiating into the waveguide (Γ_r) and the non-radiative (Γ_{nr}) part which is the losses to the local environment of the qubit. When driven through a waveguide the qubit rotates around the $\hat{x}$ axis of the Bloch Sphere at the Rabi frequency given by $\Omega = 2\sqrt{\frac{\Gamma P}{\hbar\omega_q}}$.

When applying a coherent drive on the waveguide at the qubit frequency the qubit is driven at its Rabi frequency described by the Hamiltonian

$$H = \omega_q\sigma^+\sigma^- + \Omega\sigma_x \tag{2.24}$$

where σ_x is the Pauli-X matrix $\sigma_x = |e\rangle\langle g| + |g\rangle\langle e|$. This interaction will make the qubit oscillate between its ground and excited state at the Rabi rate.

2.1.6 Dispersive Qubit readout

Reading the qubit state requires the user to affect the system. As discussed before, qubit lifetime is crucial to quantum computing, it is therefore important to design a readout system that doesn't affect the qubit lifetime. Coupling the qubit to a 2D CPW resonator is often used to read out the qubit state. The qubit is entangled with an observable of the resonator which is then probed allowing to obtain information of the qubit state through the resonator. The qubit-resonator system truncated to the first two levels is described by a Jaynes-Cummings Hamiltonian of the form

$$H = \omega_q \sigma^+ \sigma^- + \omega_r \left(\hat{a}^\dagger \hat{a} + 1/2 \right) + g \left(\sigma^+ \hat{a} + \hat{a}^\dagger \sigma^- \right) \tag{2.25}$$

In the dispersive regime $\Delta \gg g, \kappa$ with $\Delta = |\omega_q - \omega_r|$, the resonator and qubit are detuned and do not exchange energy but they affect each other frequency. In this regime, the Hamiltonian can be rewriten as

$$H_{disp} = (\omega_r + \chi \sigma_z) \left(\hat{a}^\dagger \hat{a} + 1/2 \right) + \tilde{\omega}_q \sigma^+ \sigma^- \tag{2.26}$$

Where $\chi = g^2/\Delta$ is the dispersive frequency shift of the resonator dependent of the qubit state and $\sigma_z = |g\rangle \langle g| - |e\rangle \langle e|$ is the Pauli rotation matrix around the $\hat{z}$ axis on the Bloch Sphere. The dispersive coupling also induces a frequency "Lamb shift" of the qubit $\tilde{\omega}_q = \omega_q + g^2/\Delta$. The frequency shift of the resonator allows to read the qubit state without it decaying and thus conserving its coherence time. Figure 2.4 shows the resonator magnitude and phase response when the qubit is in the ground and excited state.

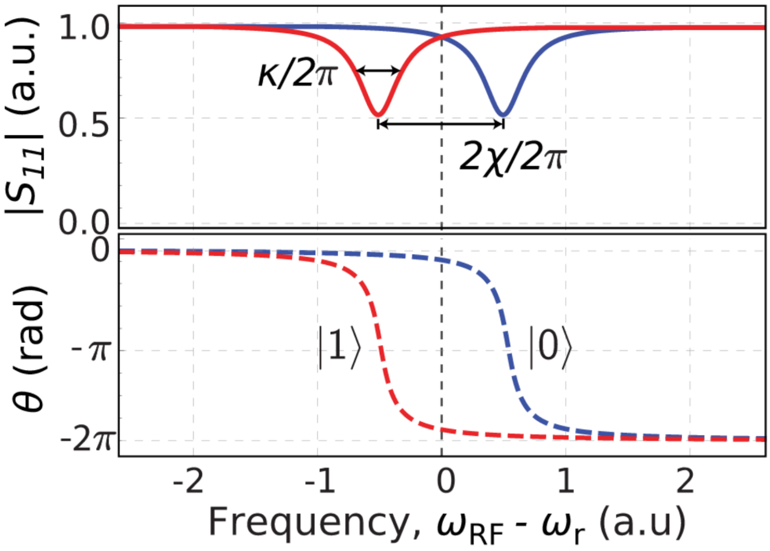

Figure 2.4: Refleted magnitude $|S_{11}|$ and phase θ of a resonator with linewidth κ dispersively coupled to a qubit with dispersive shift χ. The blue and red curves represent the resonator response when the qubit is in the ground state $|g\rangle$ and the first excited state $|e\rangle$ respectively. The separation between the blue and red curves is $2\chi/2\pi$. Taken from [12]

2.2 Autonomous Qubit Reset scheme

As previously discussed in section 1.2 resetting a qubit to its ground state after a quantum algorithm is crucial in order to start a new calculation. The qubit naturally decays to its ground state due to a complicated relaxation pathway involving ans ensemble of two-level fluctuators at the metal-oxide interfaces. As a simplication, one can consider that the qubit is weakly coupled to the environment and slowly thermalizes to it at the well known relaxation time (T_1) timescale. This process is intrinsically slow as maximum coherence time is desirable to run long quantum algorithms. During the operation of a quantum algorithm resetting a qubit faster than T_1 may be necessary.

Different approaches have been used so far to achieve a fast reset. For example, in [16], a microwave pulse drive through a resonator stimulating the decay of the qubit into the resonator achieving an excited state population of 0.2% in 500 ns. More recently a reset scheme involving parametric flux modulation of a flux-tunable qubit to induce decay into a coupled resonator achieved an excited state population of 0.08% as fast as 34 ns [17].

Our reset scheme is based on a quantum thermodynamics process in which the only necessary input signals are thermal fields. From a thermodynamics perspective thermal fields have a lower energy cost compared to microwave coherent pulses. It can also be argued that said thermal fields can be recovered from the naturally occuring thermal gradient inside the dilution cryostat. Our reset scheme is autonomous in the sense that it does not require engineered microwave pulse sequences as it operates autonomously as long as the the two photon process is allowed. Our system can also be turned ON and OFF by driving it in and out of resonance by detuning a flux-tunable qubit.

2.2.1 Working principle of the device

The cQED device designed in this thesis aims to reset a target qubit to its ground state through a two photon process between three qubits. The device consists of three qubits that we denote *Hot*, *Cold* and *Target*. The *Hot* and *Cold* qubits are coupled to waveguides in which we feed synthesized white noise corresponding to effective hot and cold temperatures. The *Target* qubit is a computational qubit that we aim to reset to the ground state with the device.

Both *Hot* and *Target* qubit are coupled to the *Cold* qubit while the *Hot* and *Target* qubits are noninteracting (see scheme in Figure 2.5a). This configuration allows for a two photon process (described in detail in sections 2.2.2 and 2.2.3) where two excitations from the *Hot* and *Target* qubits are transferred to the *Cold* qubit that absorbs them in a cascade excitation from its ground to second excited state.

This process has a net effect of removing an excitation from the *Target* qubit which allows to lower the population of the first excited state. It is also dependent on the resonant condition $2\omega_C - \alpha_C = \omega_T + \omega_H$ so the reset scheme can be turned ON and

OFF by detuning the *Cold* qutrit thus driving the system out of resonance.

The *Hot* and *Cold* qubit are coupled to waveguides with a thermal distribution corresponding to hot and cold temperatures. The qubits will thermalize to this temperatures and adopt an occupation corresponding to their waveguide temperature. Therefore the *Hot* qubit will naturally have a high excited state population while the *Cold* qutrit will have most of its population in the ground state.

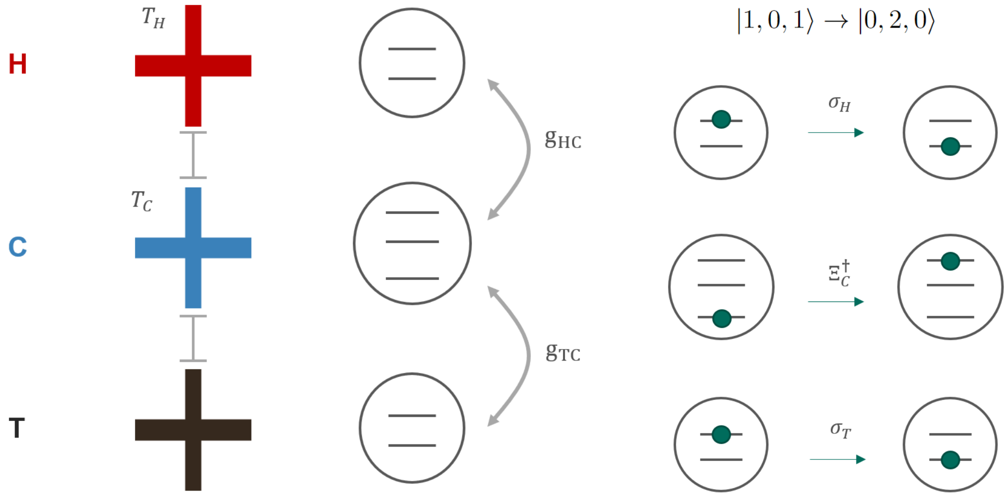

(a) Three qubit coupling scheme **(b)** Two photon process

Figure 2.5: Schematics of the working principles of the AQR device. **(a)** Three qubit coupling scheme. The *Hot* and *Cold* qubits are coupled to waveguides with effective temperature T_H and T_C. Notice how the *Cold* qutrit is a three level system and how the *Hot* and *Target* qubits are noninteracting. **(b)** Scheme showing the two photon process in which the *Hot* and *Target* qubits lose an excitation and the *Cold* qutrit is excited to it's second excited state.

2.2.2 Simultaneous excitation of noninteracting qubits

Two-photon processes have been largely studied in physics. Two-photon absorption was predicted in 1931 [18] and experimentally observed with the invention of the laser [19]. In this process an atom (or artificial atom) is excited from its ground state by the absorption of two photons whose energies sum up to the transition energy, the transition is assisted by a virtual state in the bandgap. The use of time-frequency entangled photon pairs has proven to increase the process efficiency [20–23]. Alternatively, two photons can simultaneously excite two interacting atoms under the condition 2.27 where ν_i and ω_i correspond to the photon and atom frequencies respectively [24–26]. In cQED with SC-qubits this condition enforces that the two qubits to be excited need to be coupled thus imposing strict conditions on the design and limitations with integration with other cQED elements. In 2020, Ren et al. [27] experimentally demonstrated the simultaneous excitation of two non-coupled qubits through a two-photon process involving two time-frequency entangled photons generated from the $|f\rangle \rightarrow |g\rangle$ cascade emission of a third qubit.

$$\begin{aligned} \nu_1 + \nu_2 &= \omega_1 + \omega_2 \\ \nu_i &\neq \omega_j \qquad \text{for all } i, j = 1, 2 \end{aligned} \tag{2.27}$$

Under the general condition for two-photon absorption (equation 2.27) there are four pathways for two atoms to absorb two photons as shown in Figure 2.6. The double transition probability can be calculated using second order perturbation theory by considering which photon is absorbed first. We consider two families of two pathways A_1 and A_2 (see Figure 2.6) and obtain the probabilities:

$$\begin{aligned} A_1 &= \frac{\kappa_{22}\kappa_{11}}{\nu_1 - \omega_1} + \frac{\kappa_{12}\kappa_{21}}{\nu_1 - \omega_2} \\ A_2 &= \frac{\kappa_{21}\kappa_{12}}{\nu_2 - \omega_1} + \frac{\kappa_{11}\kappa_{22}}{\nu_2 - \omega_2} \end{aligned} \tag{2.28}$$

where κ_{ij} corresponds to the coupling strength between the ω_i atom and the ν_j photon.

If we now consider that ν_1 and ν_2 are time-frequency entangled and ν_1 is emitted first we can neglect the case A_2 and obtain the simultaneous excitation probability as $P(|g_1, g_2\rangle \rightarrow |e_1, e_2\rangle) = A_1$.

In [27] the time-frequency entangled photon pair is generated by the cascade decay of a transmon from its second excited state to the ground state ($|f\rangle \rightarrow |g\rangle$). This process emits a time-frequency entangled photon pair with frequencies $\nu_1 = (E_f - E_e)/h$ and $\nu_2 = (E_e - E_g)/h$. The cascade nature of the process ensures ν_1 is always emitted first thus satisfying the condition necessary to eliminate the A_2 term.

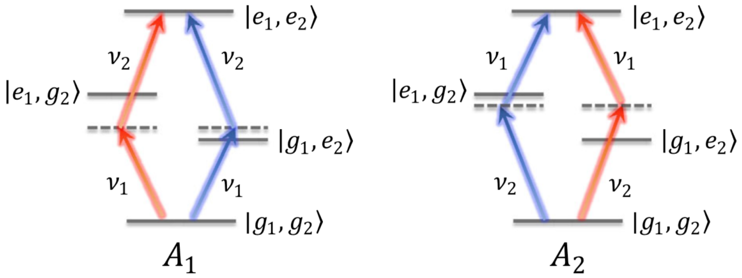

Figure 2.6: Quantum pathways for a two photon cascade absorption. A_1 and A_2 denote the cases where ν_1 or ν_2 are absorbed first. Taken from [27]

2.2.3 Three body Hamiltonian

Every light-matter interaction process has its inverse, this is shown in the Hamiltonian of the system as each term has its Hermitian conjugate (H.c.). Our qubit reset device is based on the inverse two photon process seen in Subsection 2.2.2, in essence, two noninteracting qubits simultaneously exchange an excitation with a third qubit inducing a cascade excitation to its second excited state.

The system consists of three qubits Q_1, Q_2 and Q_3 where Q_1 is coupled to Q_2 and Q_2 to Q_3 with equal coupling rates $g_{12} = g_{23}$ while Q_1 and Q_3 are uncoupled ($g_{13} \sim 0$). This system is described by a three body Hamiltonian of the form:

$$H = H_0 + H_1 \tag{2.29}$$

Where we consider H_0 the noninteracting three qubit Hamiltonian ($\hbar = 1$):

$$H_0 = \sum_{i=1,2,3} \omega_i \left|e_i\right\rangle \left\langle e_i\right| + (2\omega_2 - \alpha_2) \left|f_2\right\rangle \left\langle f_2\right| \tag{2.30}$$

Notice that we are treating Q_1 and Q_3 as TLSs while Q_3 is a three level system (qutrit) with anharmonicity α_2. The second term H_1 is the interaction part of the system given by:

$$H_1 = g_{13}\sigma_1^+\sigma_3^- + \sum_{i=1,3} g_{i2}\sigma_i^+ (\left|g_2\right\rangle \left\langle e_2\right| + \sqrt{2} \left|e_2\right\rangle \left\langle f_2\right|) + H.c. \tag{2.31}$$

The first term in equation 2.31 can be removed as $g_{13} \sim 0$. The three body Hamiltonian is therefore:

$$H = \sum_{i=1,2,3} \omega_i \left|e_i\right\rangle \left\langle e_i\right| + (2\omega_2 - \alpha_2) \left|f_2\right\rangle \left\langle f_2\right| + \sum_{i=1,3} g_{i2}\sigma_i^+ (\left|g_2\right\rangle \left\langle e_2\right| + \sqrt{2} \left|e_2\right\rangle \left\langle f_2\right|) + H.c \tag{2.32}$$

This Hamiltonian will depict the three qubit system energy landscape. The refrigeration scheme only involves the process $\left|e_1, g_2, e_3\right\rangle \to \left|g_1, f_2, g_3\right\rangle$, it is therefore convenient apply perturbation theory and transpose the problem to the subspace spanned by this two states. The process only happens under the resonance condition in which the system's energy is maintained $E = \omega_1 + \omega_3 = 2\omega_2 - \alpha_2$. The effective Hamiltonian of this process is obtained using the transformation:

$$H_{eff} = PH_1 \frac{Q}{E - H_0} H_1 P \tag{2.33}$$

Where $P = \left|g_1, f_2, g_3\right\rangle \left\langle g_1, f_2, g_3\right| + \left|e_1, g_2, e_3\right\rangle \left\langle e_1, g_2, e_3\right|$ and $Q = 1 - P$ are the relevant subspace and it's complementary. The calculation of equation 2.33 yields:

$$H_{eff} = A\sigma_1^-\sigma_3^-\Xi_2^+ + H.c. \tag{2.34}$$

where $\Xi^+ = |f\rangle\langle g|$ is the two level raising operator and the interaction strength is given by:

$$A = \sqrt{2} g_{12} g_{23} \left(\frac{1}{(2\omega_2 - \alpha_2) - \omega_1} + \frac{1}{(2\omega_2 - \alpha_2) - \omega_3} \right) \tag{2.35}$$

This parameter is crucial to the device performance as it sets the efficiency of the two photon process. Nonetheless, the performance of the device is not only dependant on this factor and a full master equation dynamics simulation with the full Hamiltonian is needed in order to properly study the device. The next section explains how these numerical simulations where performed in collaboration with the Quantum Steampunk Laboratory from The University of Maryland.

2.2.4 Expected performance from numerical simulations

As discussed before, the system dynamics are described by the master equation 1.2. This first order differential equation (ODE) can be solved numerically in order to track the evolution of the density matrix thus obtaining the dynamics of the system when let free to evolve after being set to an initial condition. The master equation describing the AQR system is:

$$\dot{\rho} = -i[H, \rho] + \sum_{i=1}^{3} \kappa_i \left[(n_{\omega_i}(T) + 1)\mathcal{D}[\hat{b}]\rho + n_{\omega_i}(T)\mathcal{D}[\hat{b}^\dagger]\rho \right] \tag{2.36}$$

Where H is the three qubit Hamiltonian in equation 2.32, n_{ω_i} refers to the thermal occupation of waveguide i and κ_i is decay rate of qubit i. In reality qubit 3, the *Target* qubit, is not coupled to a waveguide but this model describes well the intrinsic energy relaxation rate. We model this decay into the environment as a thermal bath at temperature $T_3 = 60$ mK coupled to the qubit with a decay rate corresponding to typical T_1 (energy relaxation time) values of previously measured similar transmons.

In order to simulate the refrigeration scheme the system is set to an initial state corresponding to a density matrix $\rho = \rho_1 \otimes \rho_2 \otimes |e_3\rangle\langle e_3|$ where ρ_i denotes a thermal state of temperature T_i given by:

$$\rho_i = \frac{e^{-H_i/k_B T_i}}{tr(e^{-H_i/k_B T_i})} \tag{2.37}$$

and the H_i's are the single qubit Hamiltonians given by:

$$\begin{aligned} H_{1,3} &= \omega_{1,3}\hat{b}^\dagger\hat{b} \\ H_2 &= \omega_2\hat{b}^\dagger\hat{b} + \tfrac{\alpha_2}{2}\hat{b}^\dagger\hat{b}^\dagger\hat{b}\hat{b} \end{aligned} \tag{2.38}$$

The ODE is solved for steady-state solution, when $\dot{\rho}(t) = 0$ and the population of the excited state for the *Target* qubit is computed as:

$$\langle e_3 \rangle(t) = tr\left(\left[\mathbb{1}_1 \otimes \mathbb{1}_2 \otimes |e_3\rangle \langle e_3| \right] \rho(t) \right) \tag{2.39}$$

By plotting $\langle e_3 \rangle(t)$, it is possible to track the population of the excited state of the *Target* qubit and thus characterize the refrigeration process. It is also possible to track the population evolution of other states taking part in the two photon process such as $|e_1\rangle$ and $|f_2\rangle$ in the same manner.

Figure 2.7 below shows the time evolution of different states in the system.

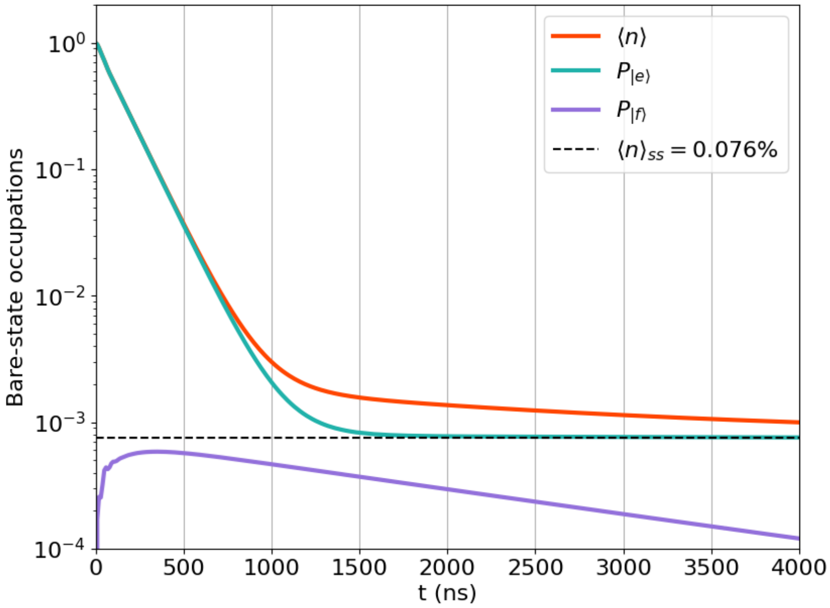

Figure 2.7: Simulation of the refrigeration scheme performance. The bare states occupations of the target qubit are plotted with respect to time with the qubit being initialized in the first excited state. The $|e\rangle$ state population (teal curve) exponentially decreases and reaches a steady state population of 0.076 % after $\sim$ 1600 ns. The excitation number (orange curve) does not completely follow the $|e\rangle$ curve as during the process some population gets transferred to the second excited state $|f\rangle$ as the purple curve shows. The qubit is no longer a TLS therefore $\langle n \rangle \neq P_{|e\rangle}$.

The simulations were run for varying device parameters, thus helping optimizing the device performance. The final optimal parameters extracted from the simulations are collected in table 4.1.

The design of the device is centered around replicating this values on the cQED platform. The following section explains in detail the design process.

3

Methods

Having understood the system from the theoretical point of view, the experimental realization starts by designing and producing a device replicating the theoretical optimal parameters in table 4.1. To achieve this a cQED superconductive circuit has to be designed with the help of electrostatic simulations. Once the device is fabricated the parameters are characterised in order to confirm the design. This Chapter is focussed on the discussion of the simulation and experimental methods used along this project.

3.1 cQED design

Designing a superconductive circuit requires precise modelling and simulation of its components. Some parts such as the qubits and waveguides are well described by a lumped element model while others such as resonators need to be studied as distributed elements. The following sections describe the methods used in both cases.

The general process flow to design and characterise cQED devices is shown in Figure 3.1.

3.1.1 Lumped element design

Qubits and waveguides are well described as lumped elements. Take for example a qubit coupled to a waveguide with the circuit diagram in Figure 3.2 below.

The waveguide is a tranmission line with a characteristic impedance Z_0 and is connected to the measurement electronics which has an effective impedance of 50 Ohm. If the waveguide is designed such that its characteristic impedance $Z = \sqrt{L/C}$ is matched to the 50 Ohm of the measurement electronics the impedance to ground of the waveguide is simply the one of the resistor. The waveguide couples to the qubit capacitively with a coupling capacitance C_g. This lumped model describes the circuit with three parameters: the qubit capacitance C and Josephson energy E_J and the coupling capacitance.

In practice, cQED circuits are fabricated as 2D metal patterns on a semiconductor substrate. In this thesis, such patterns were designed on a CAD software called

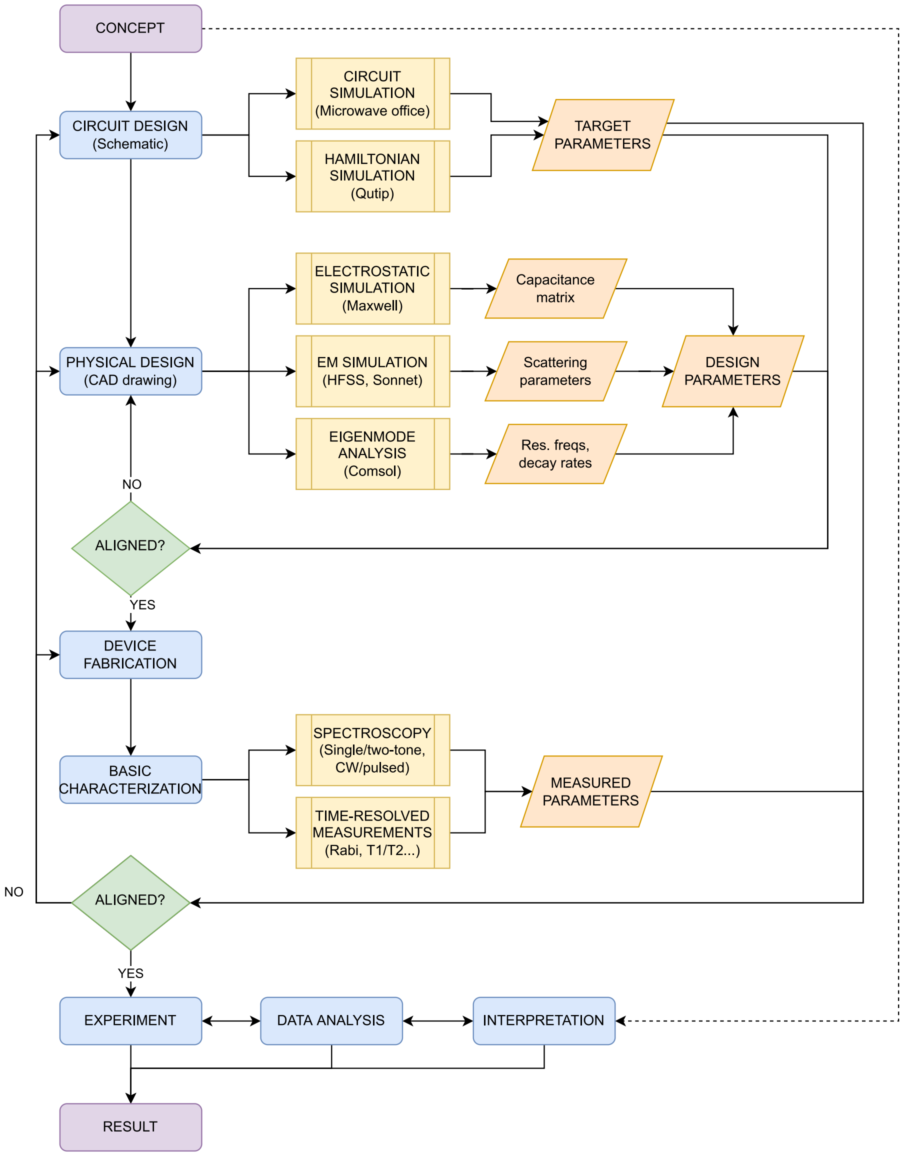

Figure 3.1: Process flow for cQED device design and characterization. Courtesy of Simone Gasparinetti.

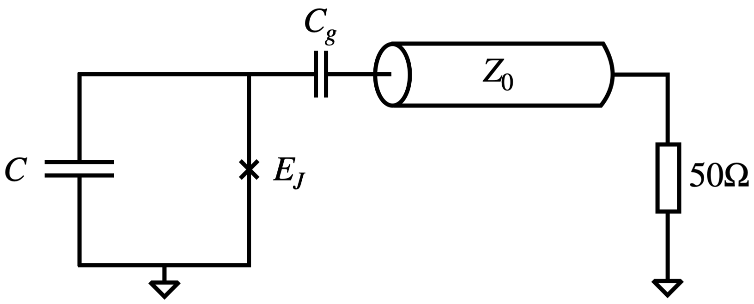

Figure 3.2: Lumped element circuit representation of a qubit coupled to a waveguide.

KLayout. Such patterns were then exported to an electrostatic simulator (Maxwell 3D) to extract the capacitance matrix of the system, i.e. a matrix showing the capacitance between all the nodes of the circuit.

The capacitance matrix is then exported and the lumped model analysis is treated using a quantum circuit analyser library for Python (QuCat) [28]. This Python module allows to define a quantum circuit by defining lumped elements between circuit nodes and allows to extract key parameters such as decay rates and qubit frequencies. The Josephson energy is added manually to the circuit model and chosen to obtain a desired qubit frequency.

The design process flow is a positive feedback loop with the following steps:

- Create a tentative device design on CAD software.
- Simulate the capacitance matrix with an electrostatic solver.
- Export and treat the simulation results using a quantum circuit analyser.
- Analyse the results and feed back for next design cycle.

3.1.2 Distributed element design

The device contains a readout resonator needed to dispersively read the *Target* qubit state. The resonator is a floating coplanar waveguide not connected to the control electronics. Its distributed nature does not allow to model it as a lumped element as seen before.

The equivalent circuit of a $\lambda/2$ readout resonator capacitively coupled to a qubit is shown in Figure 3.3.

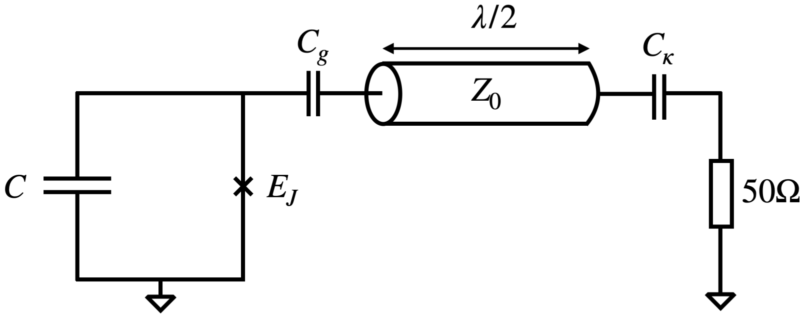

Figure 3.3: Circuit diagram of a qubit coupled to a $\lambda/2$ resonator.

Contrary to the waveguide, the resonator is a finite length transmission line and therefore we cannot treat is as a lumped element anymore. This floating piece of waveguide couples capacitively to the qubit and either capacitively or inductively to a 50 Ohm output waveguide. For this device we decided to read-out with reflection spectroscopy with capacitive coupling on a $\lambda/2$ resonator. This configuration allows to simulate the capacitive network in the same manner as with the qubits and waveguides and use a hybrid approach by obtaining the resonator frequency with an eigenmode solver (Ansys HFSS). The decay rate of the resonator into the waveguide can be calculated using a semi-classical approach described in detail in Appendix B of Marek Pechal's thesis [29]. Under this approach the decay rate κ is calculated as:

$$\kappa = \frac{2}{\pi}\tilde{\omega}_r^3 C_\kappa^2 Z_0 Re\left[Z_{env}\right] \tag{3.1}$$

Where $\tilde{\omega}_r = \omega_r - \frac{1}{\pi}\omega_r^2 C_\kappa Z_0$ is the shifted frequency of the resonator due to the coupling with the waveguide. The frequency of the resonator is the result of the eigenmode simulation. The capacitive coupling to the qubit is given to a first approximation by:

$$g = \frac{C_\kappa}{2\sqrt{CC_r}}\sqrt{\omega_q\omega_r} \tag{3.2}$$

Where C_r is the capacitance to ground of the resonator.

3.1.3 The device

The three qubit device was designed employing the design techniques recently discussed. The final device design is shown in Figure 3.4.

Figure 3.4 shows the *Hot* and *Cold* qubit-waveguide systems are colored in red and blue. The third, *Target*, qubit is colored in black and has a $\lambda/2$ resonator coupled to it. A closer look of principal elements of the device is shown in Figure 3.5.

The *Target* qubit is nominally identical to the typical transmon dimensions used in the community. The targeted parameters from the theoretical calculation require that the *Cold* qubit couples equally to the *Target* and *Hot* qubits. For this reason we designed the *Hot* qubit as a typical transmon as well. This leaves us with the *Cold* qubit that will be designed around obtaining the theoretical parameters. The *Cold* qubit should be designed in a way that it couples strongly and equally to both other qubits. The *Cold* qubit should also couple strongly to the *Cold* waveguide. As shown in Figure 3.5, the *Cold* qubit is designed as an elongated cross, whose vertical arms extend along the arms of the two other qubits. This proximity along a long distance between the qubits provides a large capacitance between the qubits, thus increasing the coupling between them. Recall equation 2.20:

$$g = \frac{1}{2}\sqrt{\omega_1\omega_2}\frac{C_g}{\sqrt{C_g + C_{\Sigma_1}}\sqrt{C_g + C_{\Sigma_2}}}$$

From this Equation, we can see how the coupling strength is proportional to the coupling capacitance C_g (capacitance between the two transmon islands). Due to the symmetry of the design we expect that to get the same coupling strength with the *Hot* and *Target* qubits we need the same coupling capacitance. This is not entirely true as even tho the *Hot* and *Cold* qubits are nominally identical capacitively they

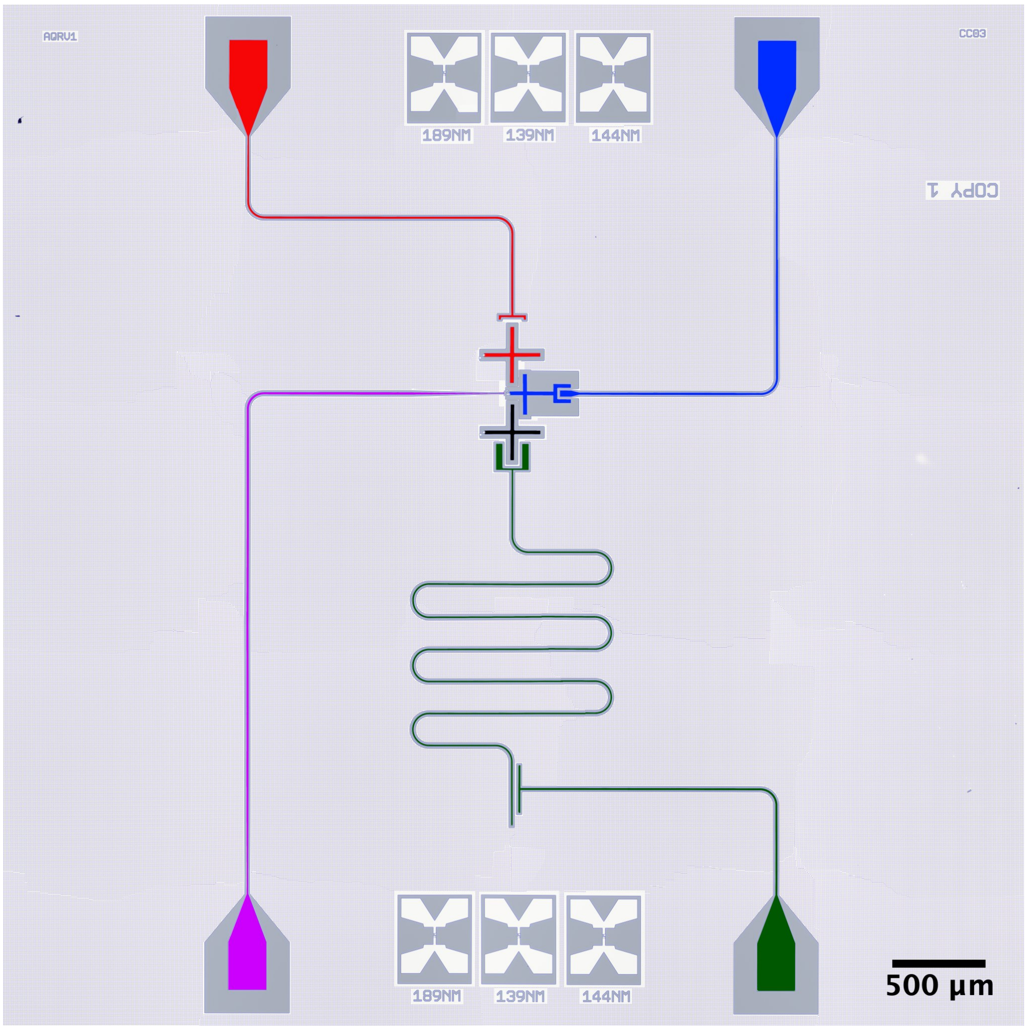

Figure 3.4: False color microscope image of the fabricated AQR device. The red and blue coloring denotes the hot and cold waveguide and qubit respectively. The *Target* qubit is colored in black and its readout resonator in green. The flux line used to tune the frequency of the *Cold* qubit is colored in purple. Many thanks to Andreas Nylander for helping capture this image.

will have different frequencies from their different JJ size. The $\sqrt{\omega_1\omega_2}$ term will introduce a variation in the coupling rate that we compensate by making the vertical arms of the *Cold* qubit of different length.

In order to achieve a high decay rate of the *Cold* qubit into its waveguide while protecting the other two qubits from decaying into it, we designed the *Cold* qubit so it would 'hug' the waveguide. This design takes care of both problems as it allows to use a smaller waveguide that will not couple to the other qubits while providing a large surface area between the qubit and waveguide for a strong coupling. This is not a usual design as in general waveguides wrap around the qubits and not the opposite, as for the *Hot* qubit and its waveguide. The extension of the ground plane around the *Cold* qubit allows to correct the anharmonicity of the qubit to match it to the targeted value.

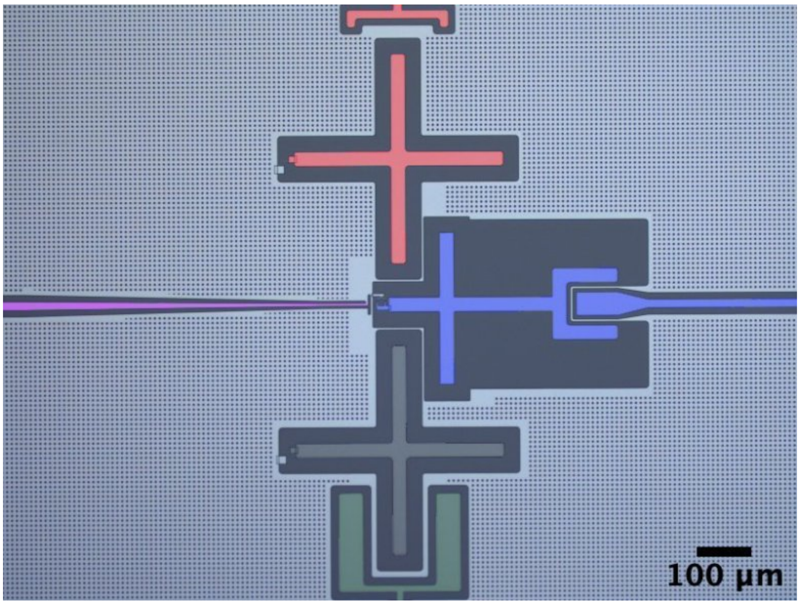

Figure 3.5: False color optical microscope image showing the principal elementns of the AQR device.

As discussed before, the *Cold* qubit is made frequency tunable through the addition of a SQUID coupled to a flux line. A close-up microscope image of the SQUID and flux line are shown in Figure 3.6.

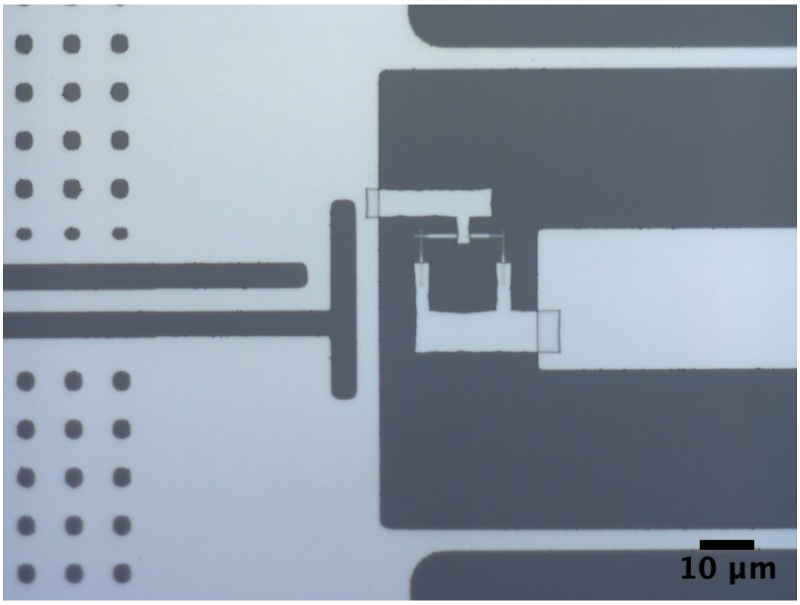

Figure 3.6: Optical microscope image showing the SQUID and flux line arrangement.

The flux line is a 50 Ω waveguide shorted to the ground close to the SQUID, the current flow going to the ground will induce a flux threading the SQUID and thus changing the Josephson energy i.e. the qubit frequency.

3.2 Cryogenic experiments

3.2.1 Experimental setup

The cryogenic experiments in this thesis were performed in a Bluefors LD dilution cryostat operated at base temperature ~ 8 mK. This temperature is past below the critical temperature of Aluminium which allows us to reach the superconducting regime and decrease the thermal fluctuations below the transition frequencies of our system. A second important characteristic of a dilution cryostat is its magnetic field shielding. This aspect becomes very important when the system contains flux tunable elements as in our case as this would introduce undesirable fluctuations in qubit frequencies.

The milliKelvin temperatures inside the refrigerator are reached by mixing two Helium isotopes in a low pressure chamber. For more details, the reader should refer to Bluefors website [30]. In order to perform microwave measurements from room temperature electronics outside the cryostat, we need to connect cables from the equipment to the input ports of device. In order to suppress the thermal noise from room temperature and intermediate temperature stages propagating through the cables, the input lines are highly attenuated at different temperature stages according to the thermalization power of each stage. The signal is low-pass filtered at 8 GHz at the mixing plate (coldest stage of the cryostat) the device in order to remove high frequency radiation that can cause quasiparticle tunneling through the JJs. The output signal of the device is then sent back to the room temperature electronics with amplification along the way (a HEMT cryogenic amplifier and a room temperature amplifier). In order to be able to perform reflection measurements on a single port of the device the input and output lines are joined with a cryogenic circulator, a non-linear electronic component that discriminates the signal depending on its propagation direction. This allows to make sure that the reflected signal from the device goes only into the output line and that the input signal does not leak into the output line before reaching the device.

Figure 3.7 below shows the wiring diagram inside the cryostat. The diagrams that will follow explaining the experimental setups correspond to the room temperature electronics connected to the input and output lines in Figure 3.7

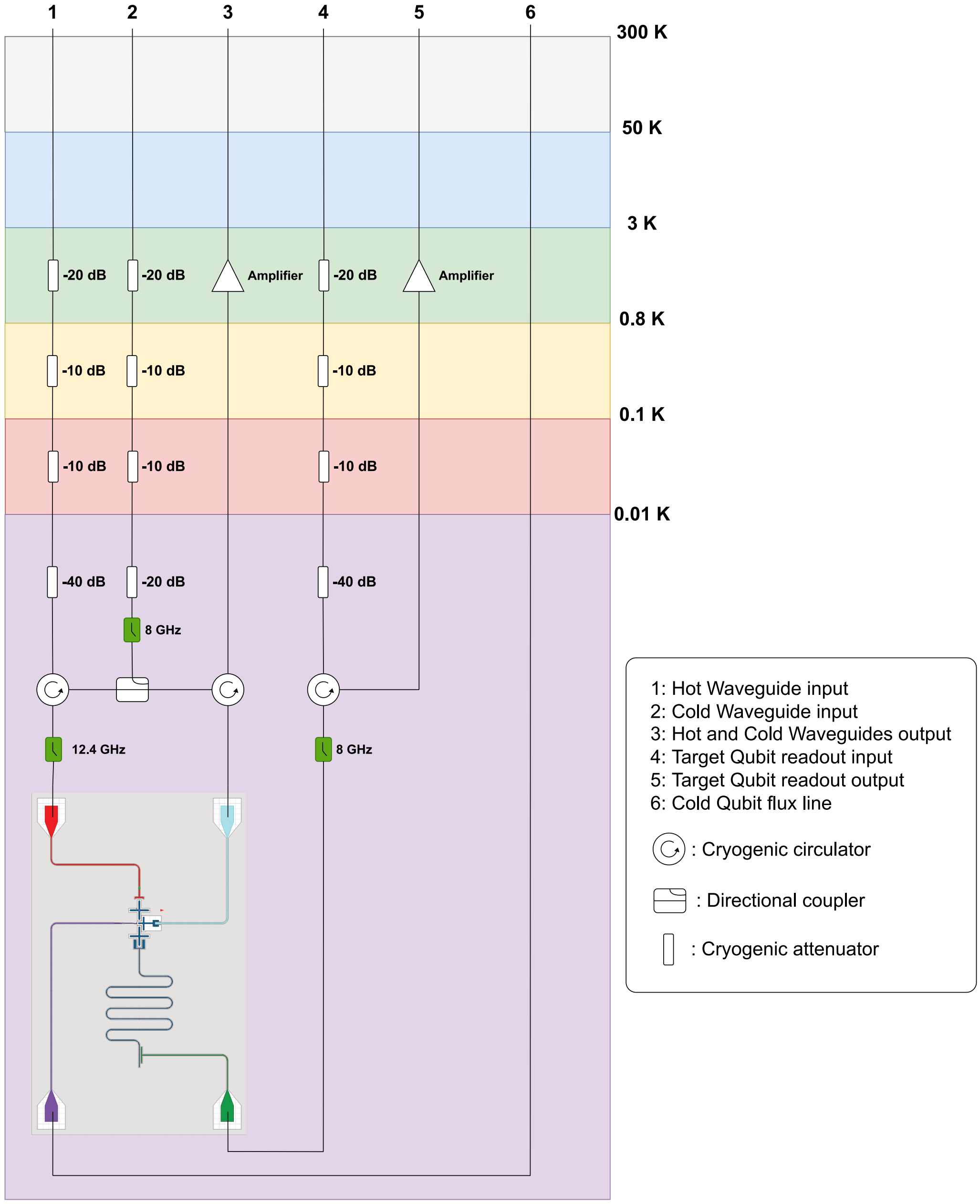

Figure 3.7: Wiring diagram of the experimental setup inside the cryostat. Following diagrams in this thesis are correspond to the room temperature electronics added to this setup.

3.2.2 Device characterisation

In order to confirm that the fabricated device matches the simulation one needs to characterize the main parameters of the device. These are the different techniques used to characterise each parameter.

3.2.2.1 Qubit-Waveguide decay rates

The decay rate of a qubit into a waveguide relates to their coupling strength. The refrigeration scheme is most efficient with the parameters in Table 4.1. In particular, we notice a much larger decay rate between the *Cold* qubit and its waveguide compared to the *Hot* qubit.

As seen in section 2.1.5, the reflection coefficient of a qubit at the end of a waveguide under a coherent drive is given by equation 2.23.

This measurement can be performed using a Vector Network Analyser (VNA). This instrument measures the scattering parameters of an electrical circuit by outputting a long coherent pulse with fixed frequency and recording the system response to input signal. In our case, we can connect one port of the VNA to the input line of the waveguide and the other port to the output line of the waveguide. The cryogenic circulator separating the two lines allows to separate the input and output signals of the waveguide. The VNA can sweep different frequency and power ranges, thus providing the reflection coefficient curve seen in equation 2.23. The experimental data can then be fitted numerically to equation 2.23 allowing to obtain the value of Γ_r, the decay rate of a qubit into a waveguide.

Depending of the power applied to waveguide, the reflection response will be different. There are three important power regimes:

- Low power: At low powers, the qubit is excited to a very small degree and can be approximated as a resonator. It scatters the incoming field in such a way that results in full reflection with no change in magnitude but an almost full 2π phase swing at the qubit frequency.

- 'Magic Power': With increasing power, the coherently scattered field out of phase with the incoming field increases. At this specific power, the scattered field has almost the same amplitude as the incoming field which destructively interferes with the reflected signal at the waveguide termination and therefore creates a strong suppression in the magnitude of the reflected field.

- High power: At higher powers, the incoming field is much larger that the out of phase signal ´scattered by the qubit known as saturation, because it cannot scatter more than a single photon. The incoming field is almost completely reflected with the same magnitude and no phase difference by the waveguide termination with negligible effect of the qubit.

3.2.2.2 Qubit-Qubit coupling rates

As seen in Subsection 2.1.4, the Hamiltonian of two coupled qubits is given by a Jaynes-Cummings Hamiltonian as in equation 2.18. In order to extract the eigenstates of the system, the Hamiltonian is diagonalized under the Bogoliubov approach in which the new eigenenergies (the dressed energies) are given by

$$
\begin{aligned}
\tilde{\omega}_1 &= \frac{1}{2}\left(\omega_1 + \omega_2 - \sqrt{\Delta^2 + 4g^2}\right) \\
\tilde{\omega}_2 &= \frac{1}{2}\left(\omega_1 + \omega_2 + \sqrt{\Delta^2 + 4g^2}\right)
\end{aligned}
\tag{3.3}
$$

The frequencies of the qubits are shifted due to the coupling. In the case of the zero detuning ($\Delta = 0$), the separation between the two dressed states is given by $\tilde{\omega}_2 - \tilde{\omega}_1 = 2g$. If one or both of the qubits are flux tunable in a range allowing the zero detuning condition, it is possible to measure the avoided crossing of the two dressed modes and obtain the coupling rate between the two qubits.

This measurement is best performed using a VNA connected to the input and output lines of a waveguide coupled to a qubit. By scanning a large frequency range and sweeping the DC voltage provided to the frequency-tunable qubit, one can track the qubit frequency with respect to flux and observe the avoided crossing between the two dressed states. The coupling rate is then given by the separation of the two branches.

3.2.3 Time domain measurements

Time domain measurements allow to study the dynamics of a cQED system by probing and recording the system's response to signal pulses. This section explains the methodology behind the time-domain measurements used in this thesis.

3.2.3.1 Dispersive readout through a resonator

Measuring the *Target* qubit state is essential to characterize the device performance. This qubit is dispersively coupled to a readout resonator as discussed in Subsection 2.1.6. In order to read the qubit state, we send a square pulse with a carrier frequency equal to the resonator frequency. The local oscillator (LO) is not capable of creating short pulses with carrier frequencies in the microwave regime; for this reason, we use the LO as a continuous microwave tone and we multiply the signal with an envelope of carrier frequency IF with the help of a microwave IQ mixer. An IQ mixer is a non-linear electronic component with four ports: LO, RF, I and Q that allows to frequency convert a signal by multiplying it with a sinusoidal continuous wave. The I and Q ports carry the same signal at the same frequency (IF) but the Q port has a $\pi/2$ phase shift. The mixer can operate in two distinct configurations, upconversion and downconversion. Upconversion consist of using the I and Q ports as input and the RF port as output. The signal coming out of the RF port will be upconverted from a frequency of f_{IF} to $f_{LO} \pm f_{IF}$ which are denoted as the left ($-$) and right ($+$) sidebands. Downconversion, on the other hand, consists of using the RF port as input and IF as output, the signal is downconverted from f_{RF} to $f_{RF} - f_{LO}$, in this case we only consider the left sideband as usually $f_{RF} \sim f_{LO} \gg f_{IF}$ and the right sideband is far away and easily filtered out.

Figure 3.8 shows the basic experimental setup used for time domain measurements. Mixers are used in upconversion mode at the resonator input in order to manufacture a square pulse with a carrier frequency $f_{LO} - f_{IF} = f_r$. This square pulse will be scattered back by the resonator and downconverted at the output line by a second mixer sharing the same LO. The resulting signal out of the RF port will then be downconverted to the IF frequency of the input line mixer. This step is necessary as the signal is recorded through a digitizer which has a limited sampling rate. For a given sampling rate f_s the largest frequency that can be sampled without aliasing is given by the Nyquist frequency $f_N = f_s/2$. The frequency interval between zero and f_N is called the first Nyquist zone (FNZ) and we need to make sure all the signal is in this region. In order to avoid higher frequencies folding into the FNZ and introducing aliasing artifacts in the signal, we place low pass filters after the mixer to eliminate all signal outside the FNZ.

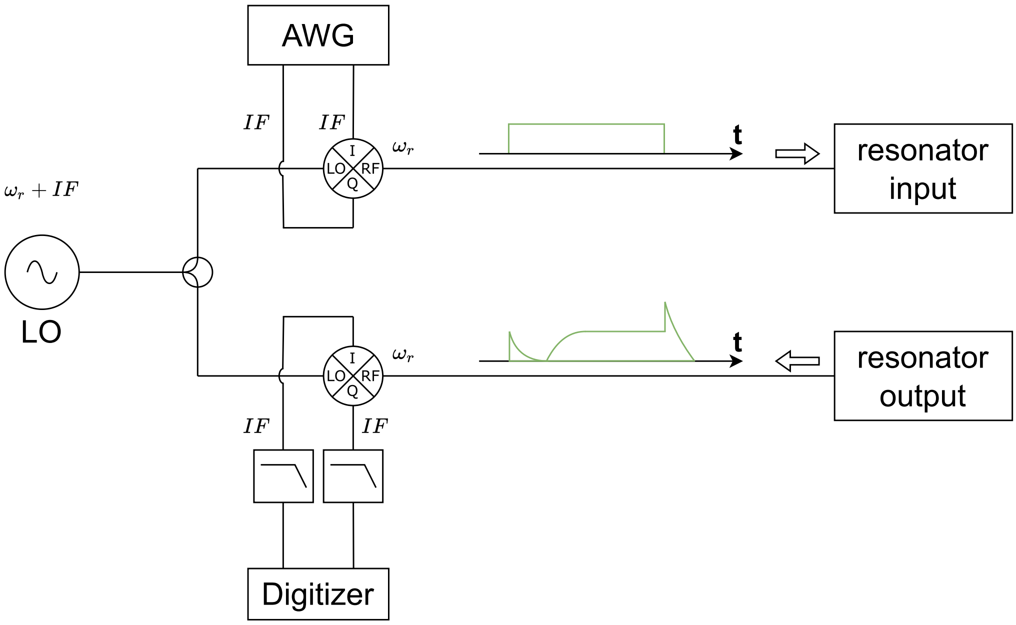

Figure 3.8: Schematic diagram of the experimental setup used for qubit readout. A local oscillator produces sinusoidal signal that is then split between the input and output branches. On the input branch the signal gets upconverted with a square envelope with carrier frequency IF produce by an AWG. The signal coming out of the RF port is a suare pulse with carrier frequency LO-IF. On the output branch the signal coming out of the resonator output is downconverted with the LO signal and the I and Q signals are collected for digitization. Before the digitizer are two low-pass filters whose function is to suppress all signal outside the first Nyquist zone of the digitizer.

3.2.3.2 Driving the qubit

The resonator can also be used to drive the qubit as an X gate, rotating the qubit state by a given angle θ around the $\hat{x}$ axis on the Bloch sphere. A pulse at the qubit frequency is sent to the resonator, which will not interact with the resonator as they are highly detuned but will resonate with the qubit inducing a population exchange between the $|g\rangle$ and $|e\rangle$ states. For a detailed derivation, the reader should refer to [31]. The Hamiltonian of a qubit driven at a frequency ω_d with amplitude A during a time t is

$$H = \omega_q \sigma^+ \sigma^- - A\cos(\omega_d t)\sigma_x \tag{3.4}$$

Assuming the qubit is in its ground state before the drive and solving the Schrödinger equation with the Hamiltonian in equation 3.4 the excited state population after the drive will be given by

$$P_{|e\rangle} = \frac{A^2}{\Omega_R^2}\sin^2\left(\frac{\Omega_R}{2}t\right) \tag{3.5}$$

Where $\Omega_R = \sqrt{A^2 + (\omega_q - \omega_d)^2}$ is the Rabi frequency at which the qubit will oscillate if continuously driven. It is clear how a coherent drive can address the qubit and manipulate its excitation state. In a more general view, the Rabi drive acts as a population inversion mechanism between the two energy levels of the qubit. Notice how when the product $\Omega_R t = n\pi$, $\forall n \in \mathbb{N}$ the population is fully inverted and we call this a π-pulse. In practice, it is more convenient to fix a certain pulse time t in the order of $\sim$ 100 ns and vary the drive amplitude A. There are twofold advantages. First, a short pulse will not allow for state decay to affect the final state as this happens on a much slower time scale of the order of ~ 10 μs. Second, a short pulse has a broader power density in the frequency domain that compensates for small detunings between the qubit and drive frequencies.

3.2.3.3 Measuring the relaxation time of a qubit

An important figure of merit of a qubit is its energy relaxation time T_1. This value is defined as the time it takes a fully excited qubit to reach the excited state population $P_{|e\rangle} = 1/e$. As seen in Section 1.3, the qubit is not a fully isolated system and decays into the environment with a given rate Γ_{env}. This decay is generally unwanted for quantum computing applications as it causes information loss and computational errors. In general, a T_1 measurement is used to measure the quality of a qubit, and in this thesis, we will use it to characterise our reset scheme.

In order to measure T_1, we will first apply a short π-pulse on the qubit and then measure it with a variable time delay after the π-pulse. This measurement allows to obtain the qubit excited state population as it decays with time. The pulse scheme for a T_1 measurement is shown in Figure 3.9.

Figure 3.9: Pulse sequence diagram of a T_1 measurement. The qubit is excited with a π-pulse and let to decay during a variable time Δt before dispersive readout.

3.2.4 Engineering thermal baths

The AQR device is designed to refrigerate through the use of thermal fields. These fields are sent to the *Hot* and *Cold* waveguides that couple to the qubits so they can couple to the thermal field.

In order to be able to tune the effective temperature of the thermal fields, we artificially synthesize them using an Arbitrary Waveform Generator (AWG). Thermal fields have a flat energy distribution in the frequency domain, i.e. a constant power spectral density (PSD). This is the characteristic spectrum of random white noise and an AWG can artificially recreate a random signal with constant PSD over a certain frequency domain. The sampling rate of the AWG (1 GHz) is not high enough to produce a random signal at the qubit frequency, therefore the AWG output signal needs to be upconverted using an IQ-mixer as discussed in Subsection 3.2.3.1.

In order to simulate a thermal bath acting on all energy levels the synthesized white noise is engineered to cover a frequency range close to 2α so that the upconverted signal centered in between the $|e\rangle$ and $|f\rangle$ frequencies covers both transition frequencies as shown in Figure 3.10. The amplitude of the thermal field can be calibrated using by a PSD measurement of Mollow triplet that relates the drive amplitude to the number of thermal photons in the waveguide. This measurement was performed during the thesis but due to hardware limitations the signal to noise ratio of the measurement was too poor to perform a proper calibration. The preliminary results involving thermal fields in the Results section are taken with un-calibrated thermal fields.

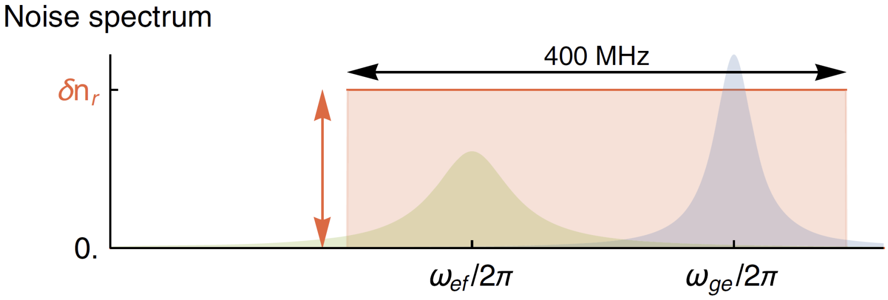

Figure 3.10: Power spectral density of the synthesized thermal field. The signal's PSD is constant over a range covering the firts two transition frequencies. The PSD amplitude can be related to the number of thermal photons in the waveguide δn_r. Taken from [32].

4

Results

This Chapter contains the main experimental results achieved during the project.

The first step before starting the main experiments was to characterize the device to confirm the design. Table 4.1 summarizes the experimental results by comparing to the theoretical target values and the simulation values.

Parameter	Target	Simulation	Experiment	Units
$\omega_1/2\pi$	5.8	5.8	5.331	GHz
$\omega_2/2\pi$	5.2	5.2	4.809	GHz
$\omega_3/2\pi$	4.4	4.4	3.727	GHz
$\Gamma_1/2\pi$	40	40.32	90.49	kHz
$\Gamma_2/2\pi$	4	3.97	6.036	MHz
$g_{12}/2\pi$	80	89.08	~ 80	MHz
$g_{23}/2\pi$	80	82.457	70.1	MHz
$\alpha_2/2\pi$	200	189	200.9	MHz
$\omega_r/2\pi$	-	6.12	6.21	GHz
$\kappa_r/2\pi$	-	250	345	kHz
$\chi_r/2\pi$	-	133	369	kHz
$g_{r3}/2\pi$	-	44	52	MHz

Table 4.1: Comparison of the theoretical, simulated and measured device parameters.

4.1 Spectroscopy

In this Section, we discuss the experimental results related to frequency domain measurements.

4.1.1 Qubit-Waveguide coupling

The device discussed in Section 3.1.3 is composed of three qubits in which two of them are coupled to a waveguide. The decay rate of the *Hot* and *Cold* qubits into their waveguide is designed for an optimal reset performance. It is therefore important to characterize these decay rates in order to confirm the design.

As explained in Subsection 3.2.2.1, the decay rate can be obtained using a reflection measurement with varying input power. The model is then fitted to the data using equation 2.23. Figure 4.1 shows the collected experimental data and Figure 4.2 shows the fitting curves used to extract the decay rates for the *Hot* and *Cold* qubits.

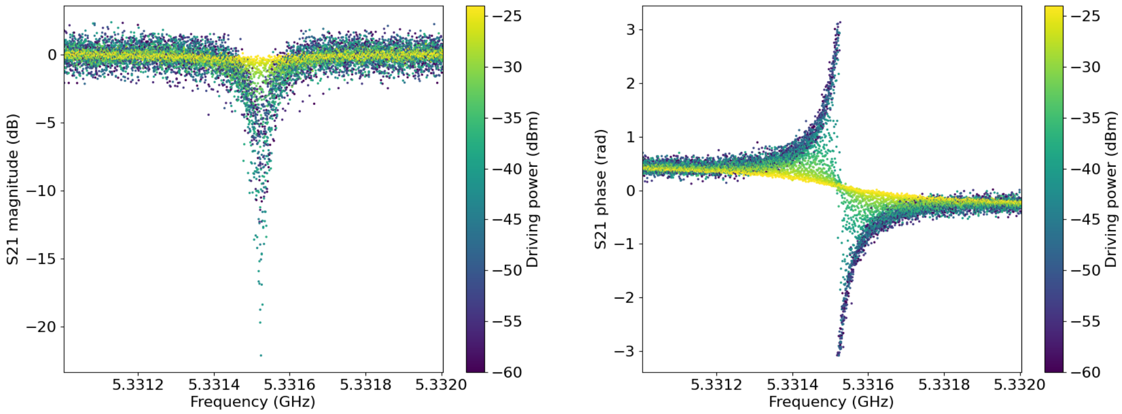

(a) *Hot* qubit power dependence in magnitude **(b)** *Hot* qubit power dependence in phase

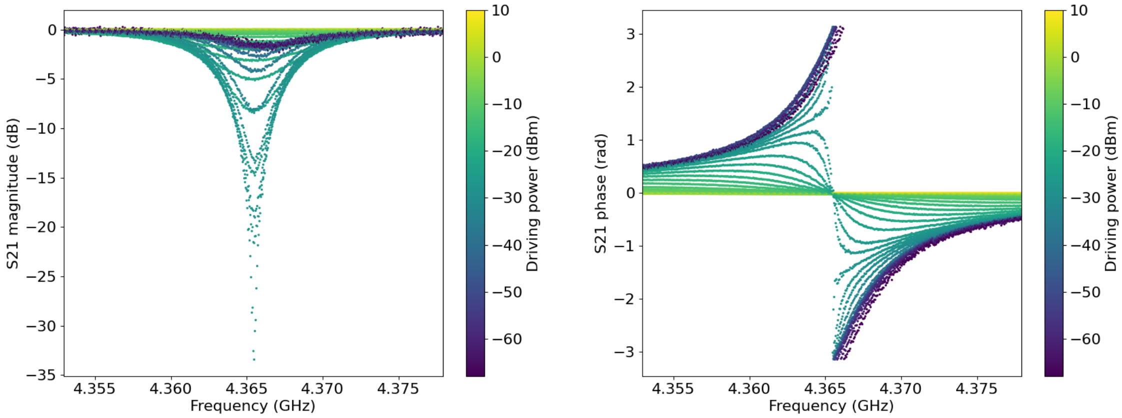

(c) *Cold* qubit power dependence in magnitude **(d)** *Cold* qubit power dependence in phase

Figure 4.1: Power dependence of reflection measurements on the *Hot* and *Cold* waveguides. As power increases the dip in magnitude increases until reaching a maximum at the so-called 'Magic Power'. For higher power values, the qubit starts to get saturated and the dip disappears.

The obtained decay rates of the *Hot* and *Cold* qubits into their respective waveguide are $\Gamma_{hot}/2\pi = 6.036$ MHz and $\Gamma_{cold}/2\pi = 90.49$ kHz. A comprehensive summary comparing the measured and simulated device parameters is given in Table 4.1.

During this experiment, we noticed that the qubit frequencies were not matching the simulations (see Table 4.1). This was due to a problem during the JJ fabrication that produced lower frequency qubits for the whole fabrication batch. This downshift in the qubit frequencies was consistent with other devices fabricated in the same fabrication round. Fortunately the resonance condition can still be achieved with these new qubit frequencies.

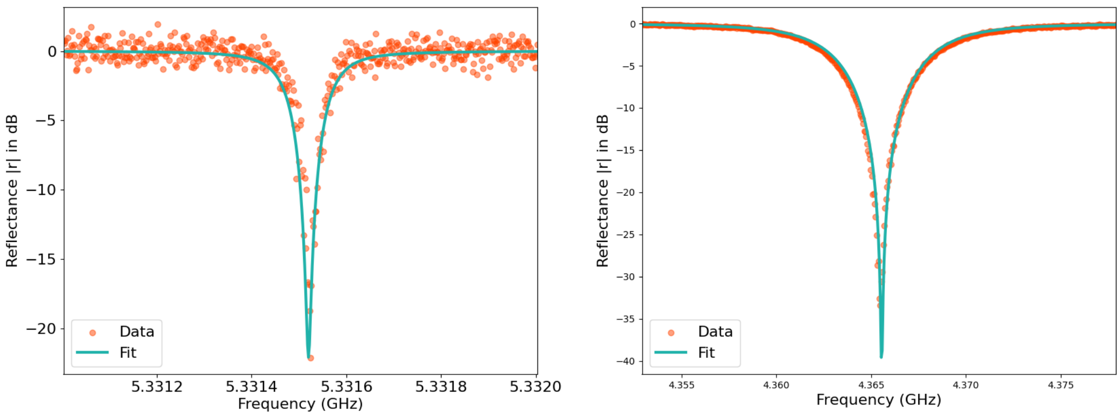

(a) $\Gamma_{hot}/2\pi = 6.036$ MHz **(b)** $\Gamma_{cold}/2\pi = 90.49$ kHz

Figure 4.2: Normalized reflected magnitude at magic power of the *Hot* and *Cold* waveguides. The orange points represent the experimental data and the teal solid line the fitting curve used to extract the decay rates.

4.1.2 Qubit anharmonicity

In order to obtain the resonant condition, it is important to characterize the *Cold* qubit anharmonicity. Recall that the resonant condition is given by $2\omega_2 + \alpha_2 = \omega_1 + \omega_3$. We have already found the *Hot* and *Cold* qubit frequencies during the decay rate characterization; the next step is to find the *Cold* qubit anharmonicity.

This is done using a pump-probe measurement in which we perform a reflection measurement at magic power as in the decay rate measurement with the addition of a continuous coherent tone at the same power at the qubit frequency. The coherent tone is supplied by a local oscillator and the reflection measurement is performed using a VNA as show in the diagram below.

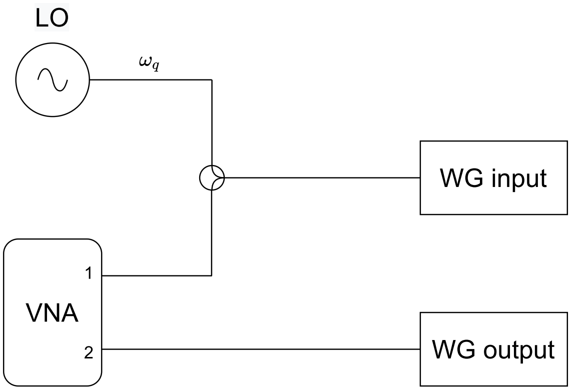

Figure 4.3: Schematic diagram of the pump-probe measurement.

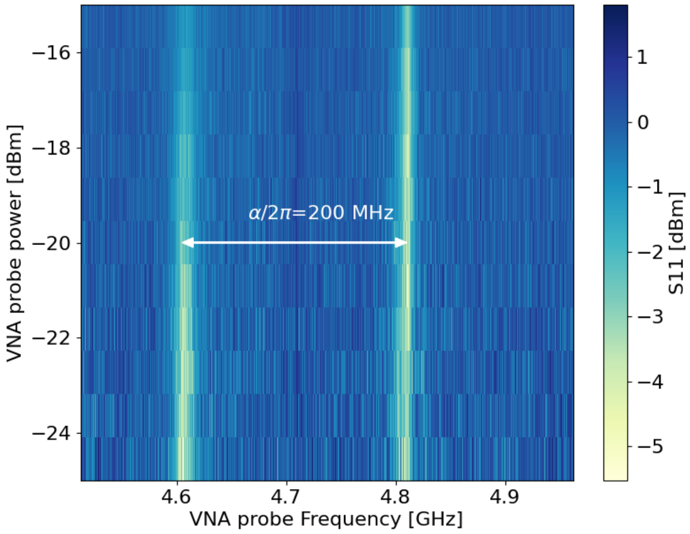

Figure 4.4: Pump-probe measurement results determining the *Cold* qubit anharmonicity.

The pump tone (at magic power) will populate the first excited state while the VNA (varying power similar to magic power) probes the $|e\rangle \rightarrow |f\rangle$ transition. The separation between both transitions gives the qubit anharmonicity. Figure 4.4 shows the collected experimental data, we measure a qubit anharmonicity of $\alpha_2/2\pi = 200$ MHz.

4.1.3 Flux dependence of tunable qubit and qubit-qubit coupling characterization

The *Cold* qubit is frequency tunable using magnetic flux threading a SQUID. The flux dependence of the qubit frequency is characterized under a reflection measurement of the *Cold* waveguide as described in Subsection 3.2.2.2.

Sweeping the flux while recording the qubit frequency using a reflection measurement at magic power (for better contrast) allows to track the qubit frequency as the flux varies. The 2D plot in Figure 4.5 shows the flux dependance of the *Cold* qubit.

As the flux amplitude increases, we can see a second branch appearing on the bottom left part of Figure 4.5. This second branch is the product of the hybridization between the *Cold* and *Target* qubits which frequencies are given by equation 3.3. As the *Cold* qubit frequency approaches the *Target* qubit frequency, the two branches form an avoided crossing where the two branches are separated by a distance $2g$ at their closest point. Figure 4.6 shows a zoomed-in section of Figure 3.3 along with the numerically extracted qubit frequencies and their minimum separation. The extracted coupling rate between the *Cold* and *Target* qubits is $g_{23}/2\pi = 70.13$ MHz. This measurement was not possible to do between the *Hot* and *Cold* qubits as the *Cold* qubit frequency cannot be swept to higher frequencies due to the commonly

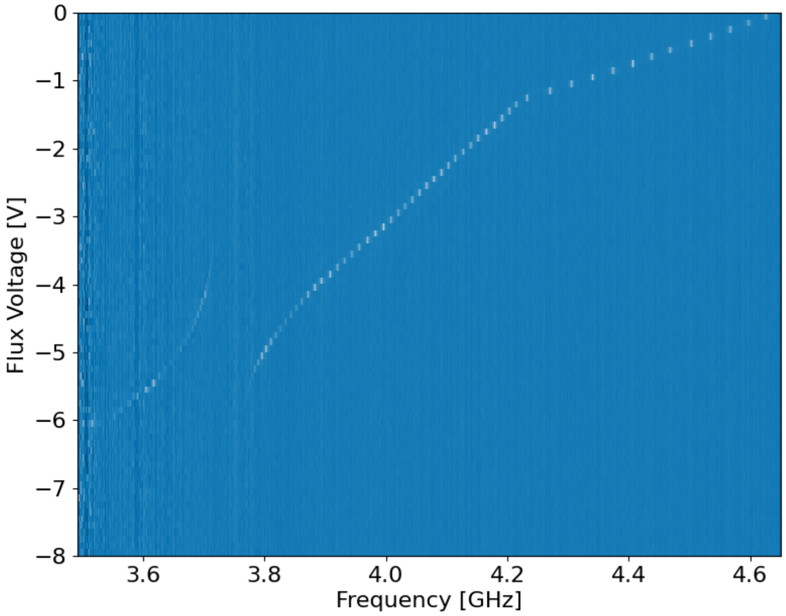

Figure 4.5: Flux dependence of the *Cold* qubit frequency showing the avoided crossing with the *Target* qubit.

denoted 'sweet spot' of the *Cold* qubit was lower than the *Hot* qubit frequency. This is a design choice as having the sweet spot at higher frequency introduces higher flux sensitivity and therefore less precision for frequency tuning.

Nonetheless, we noticed that when substituting the experimental frequencies in the QuCat analysis model, the coupling rate predicted by the analysis was matching the experimental coupling rate. Therefore, we assumed that the coupling rate between the *Hot* and *Cold* qubits would be well predicted by this model as well. We therefore expect a coupling rate $g_{12}/2\pi \sim 80$ MHz between the *Hot* and *Cold* qubits.

4.1.4 Qubit-resonator characterisation

In a latter part of the project, measuring the *Target* qubit state will become important. It is therefore important to characterize the qubit-resonator system. Some of the important parameters can be extracted from VNA measurements, in particular, the qubit and resonator frequencies, the qubit-resonator coupling and the qubit anharmonicity.

First we perform a so-called 'punch-out' measurement which consist of a reflection measurement on the resonator waveguide for varying powers. At the resonator frequency, the resonator will reflect the input signal destructively, therefore introducing a dip in the reflected magnitude, and a phase swing of nearly 2π. As we increase the input power, the resonator will 'punch-out' [31] - the induced current on the qubit coupled to the resonator will surpass the critical current of the JJ and effectively disable the qubit. We will then measure the bare cavity frequency.

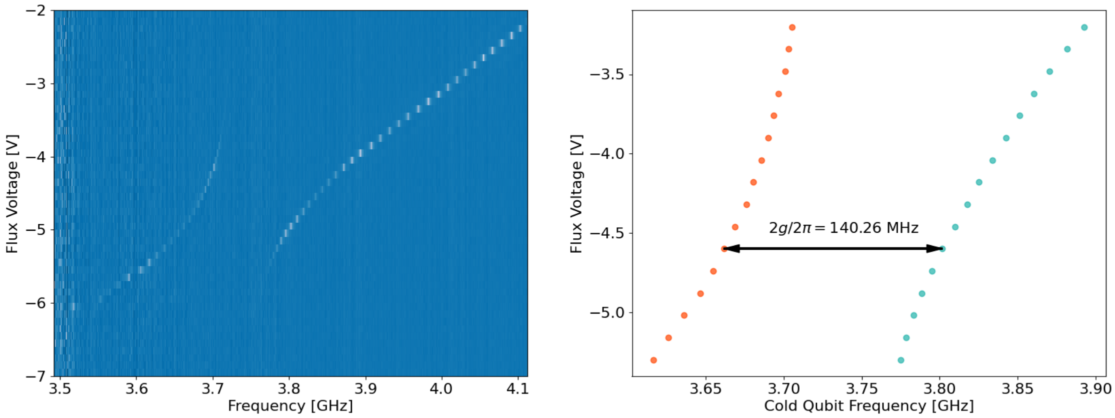

(a) Zoomed in image of the avoided crossing.

(b) Numerical interpolation of the avoided crossing

Figure 4.6: Avoided crossing between the *Cold* and *Target* qubit.

The shift in frequency of the resonator during the punch-out measurement is given by $g^2/2\pi\Delta$. In Figure 4.7, we observe a frequency shift of 106 MHz which yielded a coupling strength $g_{r3}/2\pi = 52$ MHz.

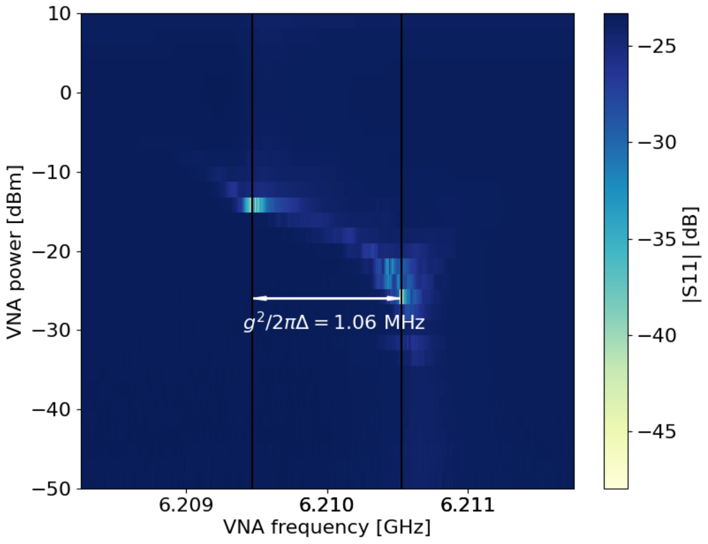

Figure 4.7: 'Punch-out' measurement showing the power dependence of the resonator frequency. At higher power the qubit mode disapears and the resonator frequency shifts to it's bare frequency.

4.2 Time domain measurements

This Section covers the results from time domain measurements.

4.2.1 Setting up a qubit readout scheme

In order to characterize the two photon resonant process we need to be able to read out the state of the *Target* qubit. The first step is to characterise the resonator frequency. A first estimation of the resonator frequency was obtained during the VNA 'punch-out' measurement. With that value noted, the setup was changed to a pulse measurement scheme as shown in Figure 3.8. Once the readout scheme was optimized the qubit frequency was found by performing a Rabi measurement as described in Subsection 3.2.3.2. The qubit frequency was then fine-tuned with Ramsey and Chevron measurements. Figure 4.8 shows a Chevron measurement on the *Target* qubit. This measurement consist of successive Rabi measurements at different qubit drive frequencies. The curve with the largest contrast in Rabi oscillations approximately corresponds to the qubit frequency. We obtained a qubit frequency of $\omega_3/2\pi = 3.727$ GHz. The π-pulse amplitude to fully invert the qubit population is obtained for 100 ns pulse with drive amplitude 60 mV.

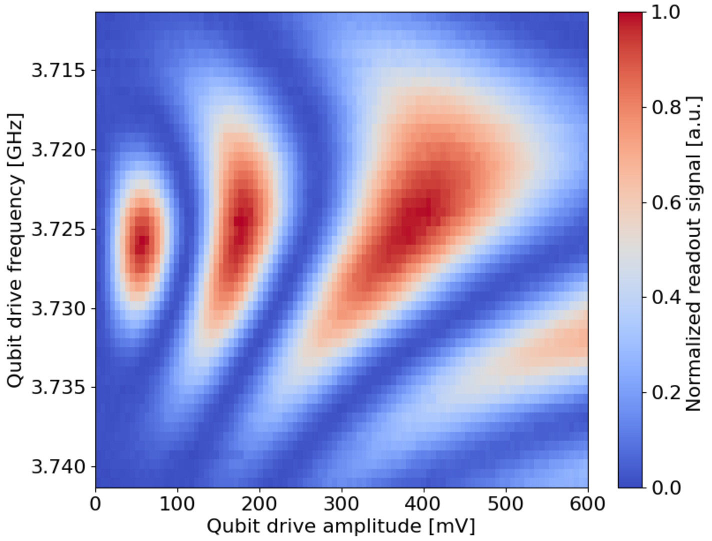

Figure 4.8: Chevron plot of the *Target* qubit.

As discussed in Subsection 3.2.3.1, the resonator frequency shifts when the qubit is excited. Figure 4.9 shows the resonator state when the qubit is in the ground state and the first excited state. We measure a dispersive shift $\chi = 369$ kHz.

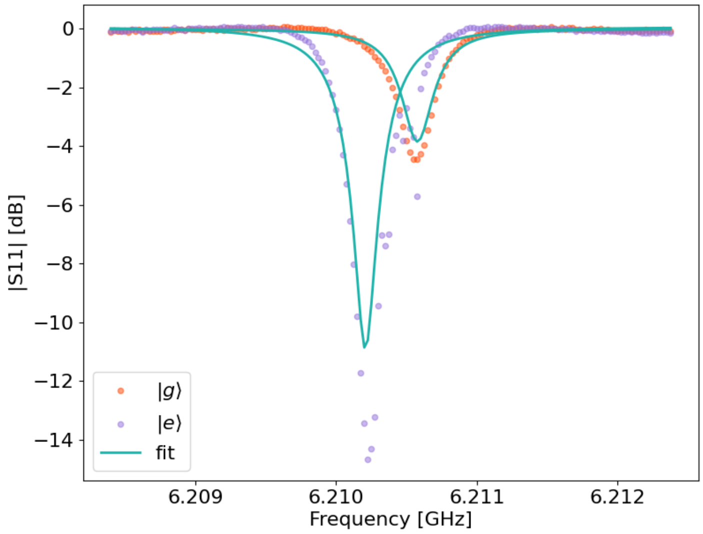

Figure 4.9: Resonator dispersive shift when the qubit is excited. The dispersive shift χ is measured to be 369 kHz

4.3 Characterization of the two photon process at resonance

Having already established a working time-domain measurement setup, we moved on to the two-photon process characterisation. By sweeping the flux on the *Cold* qubit, we can reach the resonant condition $2\omega_2 - \alpha = \omega_1 + \omega_3$. We expect a fast decay when the process is resonant as the $|020\rangle$ state decays fast into the *Cold* waveguide.

4.3.1 Rabi amplitude at resonance

In order to characterize the resonance we need to find the flux value allowing us to obtain the resonance. In order to do so we performed a gated measurement while varying the flux. The measurement consist of the following:

1. Apply a long square tone on the *Cold* qubit at its frequency at a high power. This will bring the qubit to a maximally mixed state with 50:50 population distribution between $|g\rangle$ and $|e\rangle$.
2. Apply a π-pulse on the *Target* qubit.
3. Measure the *Target* qubit state.
4. Repeat the same measurement for a new flux voltage on the *Cold* qubit.

The diagram in Figure 4.10 below illustrates the pulse scheme used for this measurement.

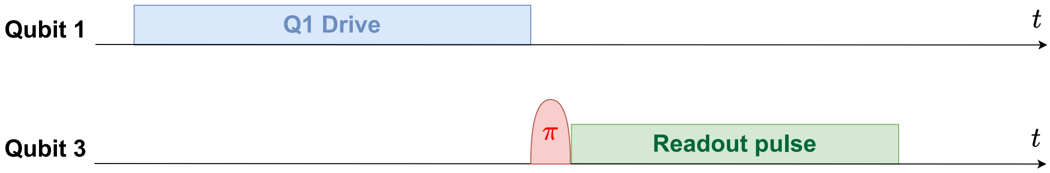

Figure 4.10: Pulse scheme diagram of the gated measurement used to locate the resonance.

While sweeping the flux we notice a region where the Rabi amplitude drops and goes back up for higher flux values as shown on Figure 4.11. This is a clear indication of the resonance.

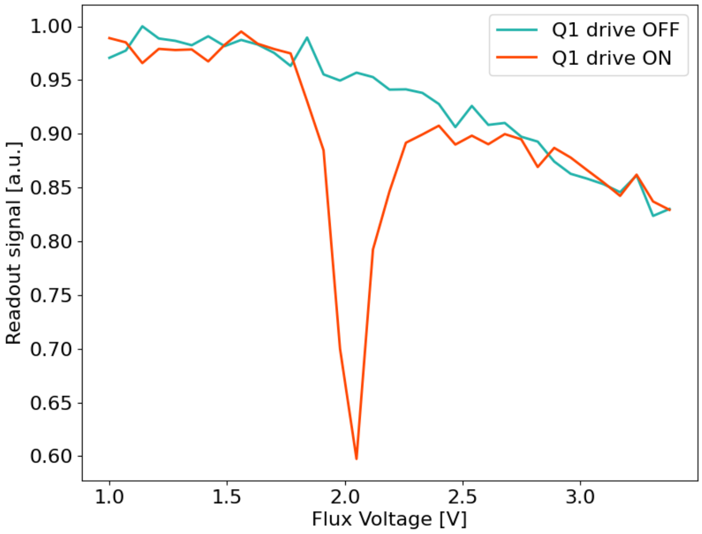

Figure 4.11: Rabi amplitude drop at resonance. The teal curve corresponds to the baseline where we don't apply the qubit drive on the *Hot* qubit.

This drop in amplitude is due to the $|101\rangle$ state hybridizing with the $|020\rangle$ state when the resonance condition is attained. When these two states hybridize, they split into the states $(|101\rangle \pm |020\rangle)/\sqrt{2}$. The $|020\rangle$ part of the hybridized state decays fast into the *Cold* waveguide due to the *Cold* qubit high decay rate and therefore, lead to a drop in the Rabi amplitude. The process is shown in Figure 4.12 below.

After the long drive pulse on the *Hot* qubit, the system is in the state $(|100\rangle \pm |000\rangle)/\sqrt{2}$ due to the *Hot* qubit being maximally mixed. Then a π-pulse is applied, making the *Target* qubit transition to the first excited state. Under resonance, the $|101\rangle$ is hybridized and the system is in the state $(|101\rangle \pm |020\rangle)/\sqrt{4} + |001\rangle/\sqrt{2}$.

The decay rate of $|020\rangle$ is given by $2\Gamma_2$ which corresponds to a relaxation time of $T_1 = \frac{1}{2\pi 2\Gamma_2} = 13$ ns. This time is faster than the delay between the π-pulse and the start of the digitization time of the readout pulse, we can therefore assume that the $|020\rangle$ component has completely decayed when we perform the readout. The final

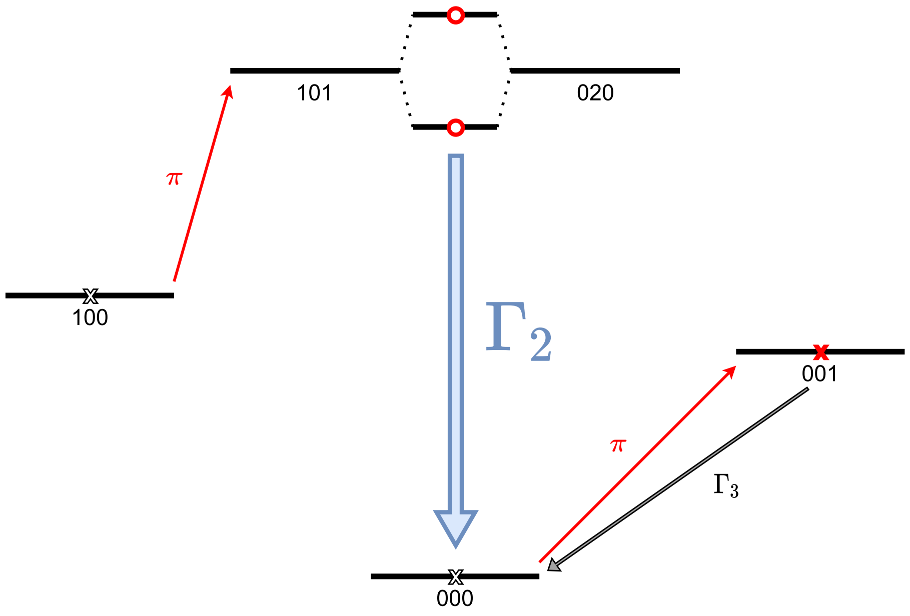

Figure 4.12: Toy model diagram explaining the Rabi amplitude drop. The crosses and circles indicate a 50% and 25% population distribution respectively. Black crosses and circles indicate the state before applying the π-pulse on the *Target* qubit and red crosses and circles represent the state after the π-pulse. Solid arrows indicate induced transitions while bi-color arrows indicate relaxation transitions.

state that is measured is $|101\rangle/\sqrt{4} + |001\rangle/\sqrt{2} + |000\rangle\sqrt{4}$. We therefore expect a 25% reduction of the *Target* qubit excited state population. Figure 4.13 shows the Rabi oscillations of the *Target* qubit on and off resonance and with and without a drive pulse on the *Hot* qubit.

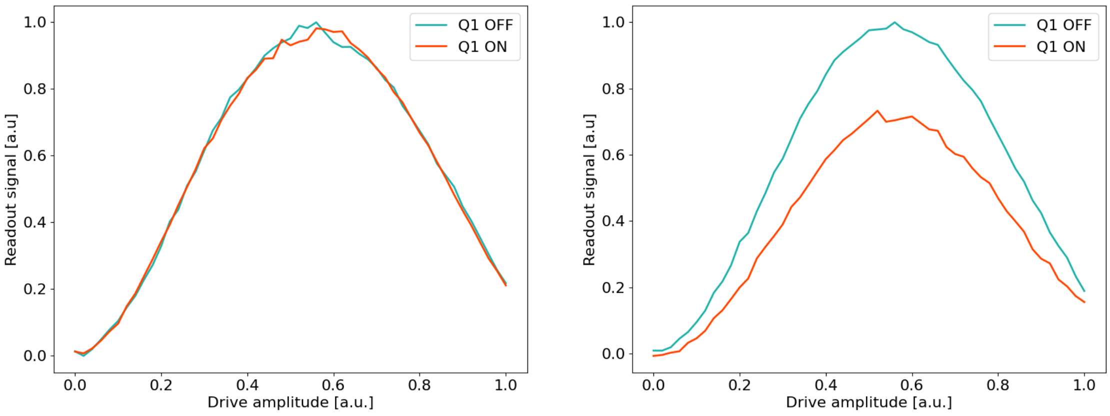

(a) Off resonant

(b) Resonant

Figure 4.13: Rabi oscillations of the *Target* qubit on an off resonance and with and without drive on the *Hot* qubit.

4.3.2 Rabi driving the resonance

Having found the resonance, we performed a new measurement similar to the gated measurement seen in the last section. In order to characterise the effect of the *Hot* qubit population on the strength of the resonance, we replaced the long drive pulse by a short pulse of varying amplitude. This allows to perform Rabi oscillations on the *Hot* qubit while we measure the *Target* qubit. The pulse sequence used for this measurement is shown in Figure 4.14.

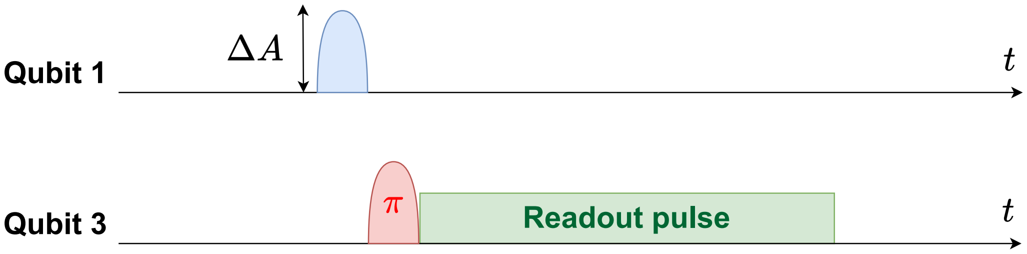

Figure 4.14: Pulse scheme diagram of the resonance characterization with Rabi oscillations of the *Hot* qubit.

This measurement allows to characterise the decrease in Rabi amplitude as a function of the *Hot* qubit excited state population. The results of this measurement are shown in Figure 4.15 below.

As we sweep the *Hot* qubit drive amplitude at resonance condition, we see Rabi oscillations corresponding to the *Hot* qubit excited state population. This is, in practice, a Rabi measurement of a qubit through a three atom interaction in which the measurement qubit is decoupled from the effectively measured qubit.

From Figure 4.15, we can obtain the optimal conditions for resetting the *Cold* qubit. In the next Subsection, we will look at the dynamics of the reset using these conditions.

4.3.3 Qubit reset dynamics of the two-photon process

Having found the amplitude needed to apply a π-pulse on the *Hot* qubit, we can now study the reset dynamics of the *Target* qubit. This is done by measuring the relaxation time T_1 of the *Cold* qubit at resonance while coherently driving the *Hot* qubit. The pulse scheme for this measurement is shown in the Figure 4.16.

Notice how we reversed the order of the qubit drive pulses, this is to ensure we are able to capture the fast decay dynamics of the resonant component. We perform the T_1 measurement with and without applying the coherent drive on the *Hot* qubit in order to compare the reset with the intrinsic relaxation time of the qubit. Notice how the *Hot* qubit is continuously driven during the waiting time of the T_1 measurement. The results of this measurement are shown in Figure 4.17.

From Figure 4.17, we can extract the relaxation time of the *Target* qubit without drive on the *Hot* qubit with a classic exponential fit $s(t) = s_0 e^{-t/T_1}$ where $s(t)$ is

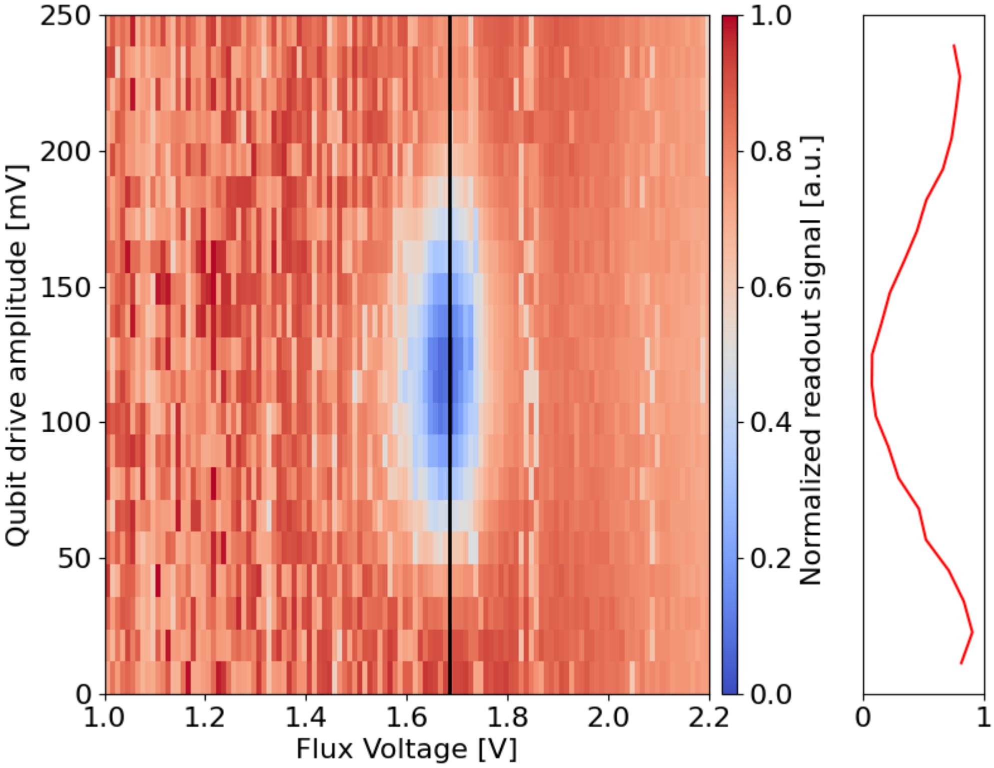

Figure 4.15: Rabi amplitude at resonance with respect to the *Hot* qubit drive amplitude with vertical cross section showing the Rabi oscillations of the *Hot* qubit.

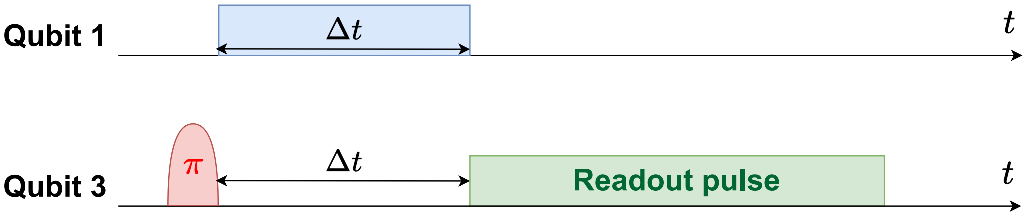

Figure 4.16: Pulse scheme diagram of the reset dynamics measurement.

the normalized readout signal. When the *Hot* qubit is not driven we measure a relaxation time of $T_1 = 21.98$ μs. This is the intrinsic relaxation rate due to the qubit decaying into the environment. Once the drive on the *Hot* qubit is turned on, we observe a much sharper decay with a characteristic relaxation time of $T_1 = 98.67$ ns.

This result can be explained following the scheme in Figure 4.18.

The coherent drive on the *Hot* qubit drives the system into the $|101\rangle$ state and due to the two photon process $|101\rangle \rightarrow |020\rangle$ it continuously rehybridizes. The effective decay rate of the process can be approximated by solving the non-Hermitian Hamiltonian of the system reduced to the $|101\rangle, |000\rangle$ basis shown in equation 4.1.

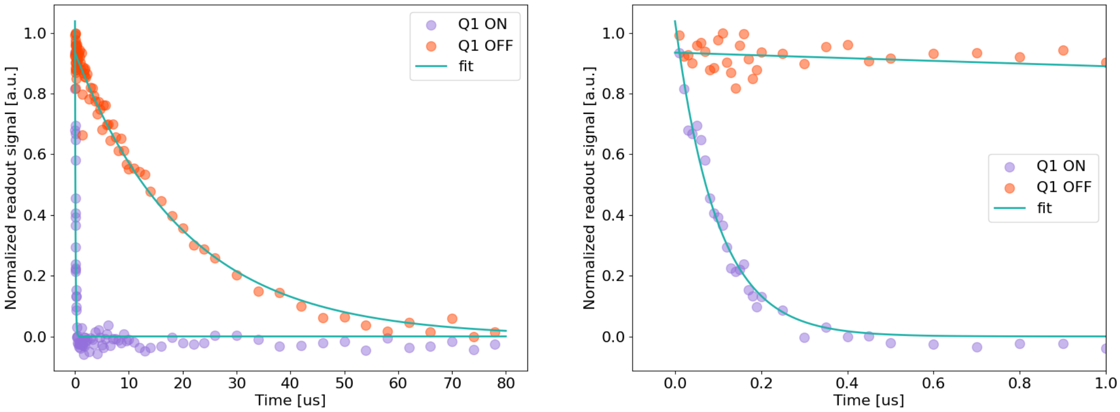

(a) Long relaxation dynamics.

(b) Relaxation in the first microsecond.

Figure 4.17: T_1 measurement on the *Target* qubit at resonance dependent on the application of a π-pulse on the *Hot* qubit.

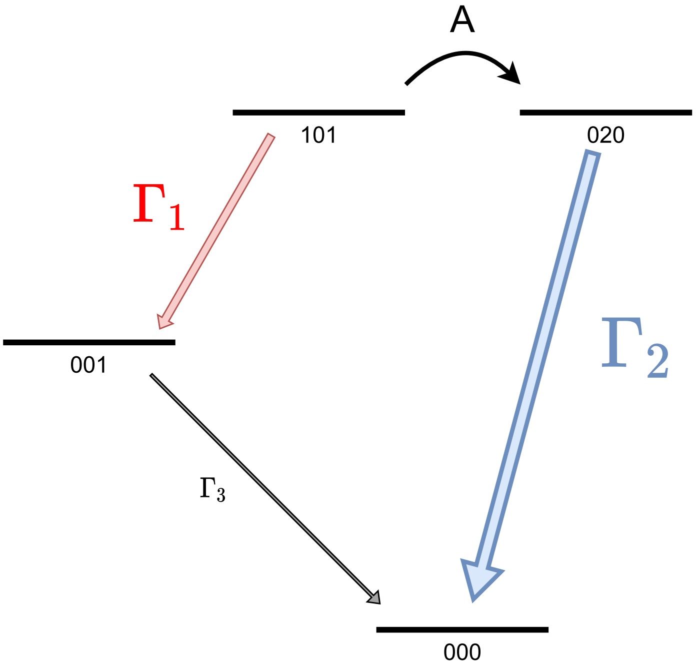

Figure 4.18: Scheme explaining the fast decay in Figure 4.17

$$H_{NH} = \begin{pmatrix} \omega_1 + \omega_3 & A \\ A & \omega_1 + \omega_3 - i\Gamma_2 \end{pmatrix} \tag{4.1}$$

Solving the Schrödinger equation for this Hamiltonian gives the time evolution of the system from which we extract the effective decay rate as:

$$\Gamma_{eff}^{theory} = \frac{1}{2}\left(2\Gamma_2 - \sqrt{-16A^2 + 4\Gamma_2^2}\right) \tag{4.2}$$

where A is the $|101\rangle \rightarrow |020\rangle$ interaction strength defined in equation 2.35. This effective decay rate calculated from the values found in Table 4.1 is $T_1^{eff,theory} = 53$ ns. The deviation from the experimentally obtained $T_1^{eff,exp} = 98.67$ ns can be explained by a possible inaccuracy in the calculation of the A term as it contains the coupling rate g_{12} which we could not experimentally measured and was obtained by extrapolation in the simulation model.

Another important figure of merit when evaluating qubit reset performance is the residual excited state population after the reset protocol is implemented. This can be experimentally measured by comparing $|e\rangle \leftrightarrow |f\rangle$ Rabi oscillations amplitudes as described in [33]. The measurement consist of comparing Rabi oscillations between the $|e\rangle$ and $|f\rangle$ states in the cases where a π-pulse has been applied previously or not. The π-pulse inverts the population between the $|g\rangle$ and $|e\rangle$ states and the $|e\rangle \leftrightarrow |f\rangle$ Rabi oscillation amplitude is a measure of the $|e\rangle$ state population. By comparing the inverted and non-inverted amplitudes on can obtain the ratio of the populations between the $|g\rangle$ and $|e\rangle$ states. If we assume negligible population in the higher energy states we can then obtain the excited state population as:

$$P_{|e\rangle} = \frac{A_{signal}}{A_{signal} + A_{reference}} \tag{4.3}$$

where $A_{reference}$ and A_{signal} correspond to the Rabi amplitudes with and without $|g\rangle \leftrightarrow |e\rangle$ population inversion. In practice, it is enough to measure only two points (the minimum and the maximum) of the Rabi oscillations in order to obtain the amplitude. The resulting pulse scheme for the residual population measurement is shown in Figure 4.19.

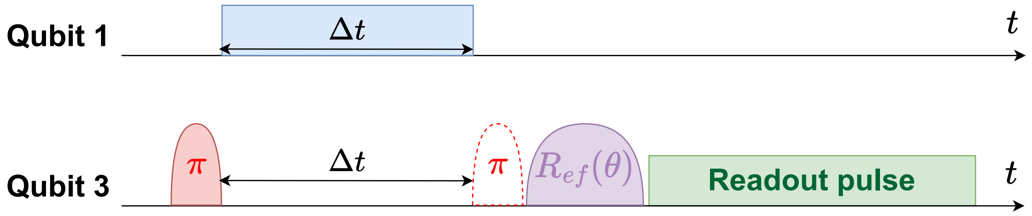

Figure 4.19: Pulse scheme used to determine the residual steady state population of the *Target* qubit. Note that the second π-pulse is conditional to the signal and reference signals.

Figure 4.20 shows a preliminary experimental result of qubit reset reaching a steady-state population below 0.2% in less than 2 μs.

The measurement shown in Figure 4.20 shows a decay slower that in Figure 4.17a. This is due to the measurement not being fully optimized for fast reset due to a time management constraint. Nonetheless, this preliminary results is already competitive

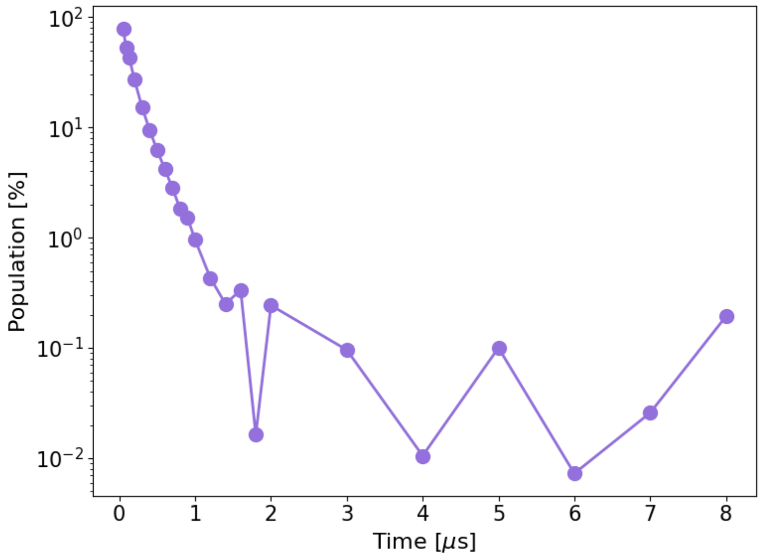

Figure 4.20: *Target* qubit residual excited state population during the reset protocol.

with most of the currently known reset schemes as shown in Figure 4.21. We expect that, when properly tuned, the system can provide state-of-the-art reset in 600ns ($6T_1$) reaching residual populations as low as 0.1%.

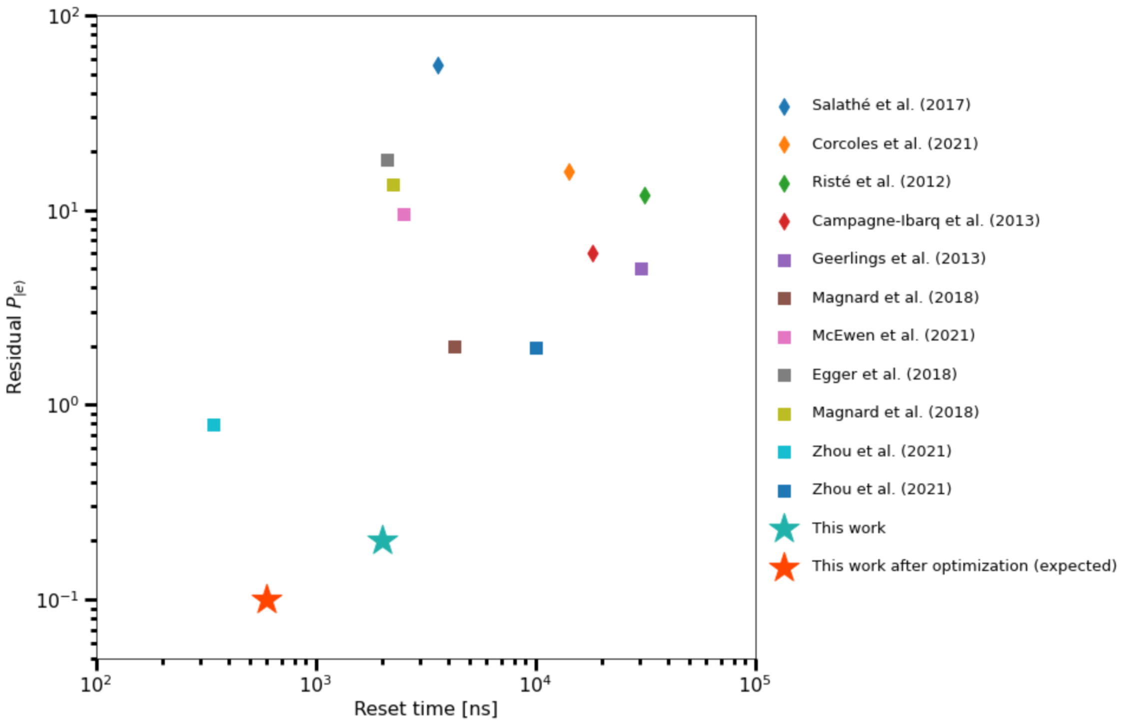

Figure 4.21: Comparison with other know reset schemes. The diamond markers represent measurement based protocols and the square markers represent non-measurement based protocols. Figure adapted from [17].

4.3.4 Autonomous qubit reset demonstration

Our last experiment showed how the *Target* qubit can be reset under resonance condition by applying a π-pulse on the *Hot* qubit. This experiment showed how population the *Hot* qubit allows for fast reset on the *Target* qubit. We now want to investigate how to render this system autonomous in the thermodynamic sense by using thermal fields instead of coherent drive on the *Hot* qubit.

In order to do so, we replaced the π-pulse drive on the *Hot* qubit by a continuous thermal field at the *Hot* qubit frequency as previously explained in Section 3.2.4. This thermal field will act a thermal reservoir to which the *Hot* qubit will thermalize, thus allowing us to fix and maintain a certain population on the *Hot* qubit during the whole reset protocol. The resulting pulse sequence for this measurement is shown in Figure 4.22.

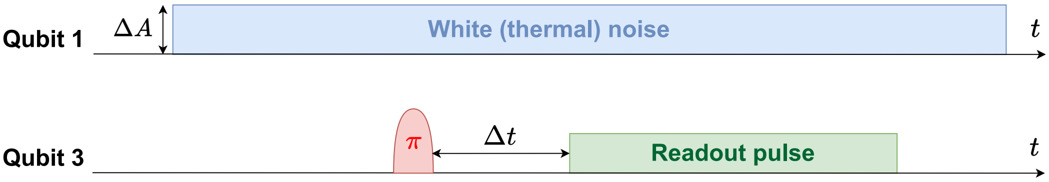

Figure 4.22: Pulse scheme diagram of the reset with thermal noise.

This measurement was repeated for varying amplitudes of thermal noise. The resulting relaxation curves are shown in Figure 4.23.

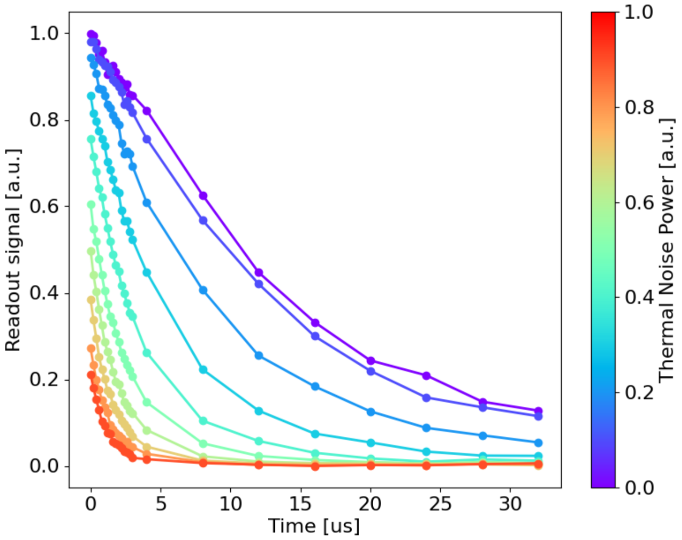

Figure 4.23: *Target* qubit relaxation dynamics with respect to applied thermal noise amplitude.

From Figure 4.23, one can observe two effects when increasing the thermal noise power. First, the initial drop in π-pulse amplitude increases for higher thermal noise power. This effect is due to a higher initial excited state population in the *Hot* qubit. Recall from Subsection 4.3.1, how under resonance condition, the Rabi amplitude drops due to the fast decay of the $|020\rangle$ part of the hybridized state. The second effect of increasing the noise power is a decrease of the relaxation time. In this case, the constant thermal drive puts the *Hot* qubit in contact with a thermal bath that constantly replenishes the excited state population on the *Hot* qubit.

As discussed earlier, the decay rate of the *Target* qubit is related to the excited state population on the *Hot* qubit. Thermal fields allow us to fix a given population on the *Hot* qubit thus directly affecting the decay dynamics of the *Target* qubit. This experiment provides early evidence of the possibility of using thermal fields to implement qubit reset.

5

Conclusion

In this project we studied a novel approach to qubit reset in which a three-body interaction between superconductive qubits is engineered to reset a *Target* qubit. The cQED device was designed employing electrostatic and eigenmode numerical simulation tools from the ground up. The design was later on confirmed through experimental characterisation. Key parameters such as coupling rates, decay rates, anharmonicities and qubit readout parameters were measured in cryogenic conditions showing good agreement with the targeted values. The two-photon process enabling the reset protocol was experimentally observed and characterised.

A first experimental demonstration of qubit reset was obtained in which we observed a sharp drop of the relaxation time. This result confirms that the engineered two photon process has a net effect of removing excited state population on the *Target* qubit. As of now, we have demonstrated a qubit reset protocol in which the only input required is a coherent tone on the *Hot* qubit, allowing the *Target* qubit to perform quantum computation freely and resetting it at will by simply applying a single microwave pulse on the *Hot* qubit.

The next natural step in this project was to replace the coherent drive tone by continuous thermal fields on the *Hot* waveguide, thus allowing continuous re-pumping of the *Hot* qubit excited state rendering the system autonomous. This experiment showed early evidence of qubit reset using thermal fields, a phenomena (to the best of our knowledge) never measured before.

This first version of the AQR device has showed promising results for qubit reset. Whether the platform can achieve refrigeration (getting the qubit colder than it would by thermalizing to the coldest bath) or not is still an open question. In order to characterise the refrigeration performance of the device the next step in the project is to perform accurate residual excited state population measurements on the *Target* qubit as we expect to reach a lower residual steady state population. Finally, a fine optimization involving carefully calibrated thermal fields on the *Hot* and *Cold* waveguides could potentially improve the refrigeration process further.

Bibliography

[1] N. Bohr, “On the constitution of atoms and molecules”, Philos. Mag. **26** (1913).

[2] W. Heisenberg et al., “Folgerungen aus der diracschen theorie des positrons”, Z. Phys. **98**, 714 (1936).

[3] M. Planck, “On the law of distribution of energy in the normal spectrum”, Ann. Phys. **4**, 553 (1901).

[4] R. P. Feynman, “Quantum mechanical computers”, Optics News **11**, 11–20 (1985).

[5] P. W. Shor, “Polynomial-time algorithms for prime factorization and discrete logarithms on a quantum computer”, SIAM Journal on Scientific and Statistical Computing **26**, 1484 (1997).

[6] F. Arute et al., “Quantum supremacy using a programmable superconducting processor”, Nature **574**, 505–510 (2019).

[7] H. J. Carmichael, *Statistical methods in quantum optics 1: master equations and fokker-planck equations*, 2nd ed. (Springer, Berlin, 2002).

[8] A. W. Glaetzle et al., “A single trapped atom in front of an oscillating mirror”, Optics Communications **283**, 758–765 (2010).

[9] M. H. Devoret et al., “Superconducting qubits”, Les Houches **79**, 443–485 (2004).

[10] D. Schuster, “Circuit quantum electrodynamics”, PhD thesis (Yale University, 2007).

[11] A. Blais et al., “Circuit quantum electrodynamics”, Reviews of Modern Physics **93**, 025005 (2021).

[12] P. Krantz et al., “A quantum engineer’s guide to superconducting qubits”, Applied Physics Reviews **6**, 021318 (2019).

[13] I.-C. Hoi et al., “Generation of nonclassical microwave states using an artificial atom in 1d open space”, Phys. Rev. Lett. **108**, 263601– (2012).

[14] I.-C. Hoi et al., “Probing the quantum vacuum with an artificial atom in front of a mirror”, Nature Physics **11**, 1045–1049 (2015).

[15] K. Koshino et al., “Control of the radiative level shift and linewidth of a superconducting artificial atom through a variable boundary condition”, New Journal of Physics **14**, 043005 (2012).

[16] P. Magnard et al., “Fast and unconditional all-microwave reset of a superconducting qubit”, Phys. Rev. Lett. **121**, 060502 (2018).

[17] Y. Zhou et al., “Rapid and unconditional parametric reset protocol for tunable superconducting qubits”, arXiv:2103.11315 [quant-ph] (2021).

[18] M. Göppert-Mayer, “ber elementarakte mit zwei quantensprüngen”, Annalen der Physik **401**, 273–294 (1931).

[19] W. Kaiser et al., "Two-photon excitation in CaF2:eu2+", Physical Review Letters **7**, 229–231 (1961).

[20] J. Javanainen et al., "Linear intensity dependence of a two-photon transition rate", Physical Review A **41**, 5088–5091 (1990).

[21] J. Gea-Banacloche, "Two-photon absorption of nonclassical light", Phys. Rev. Lett. **62**, 1603–1606 (1989).

[22] B. Dayan et al., "Nonlinear interactions with an ultrahigh flux of broadband entangled photons", Physical Review Letters **94**, 043602 (2005).

[23] A. Muthukrishnan et al., "Inducing disallowed two-atom transitions with temporally entangled photons", Physical Review Letters **93**, 093002 (2004).

[24] J. C. White, "Observation of multiphoton-laser-induced collisions", Optics Letters **6**, 242–244 (1981).

[25] G. V. Varada et al., "Two-photon resonance induced by the dipole-dipole interaction", Physical Review A **45**, 6721–6729 (1992).

[26] E. Pedrozo-Peñafiel et al., "Two-photon cooperative absorption in colliding cold na atoms", Physical Review Letters **108**, 253004 (2012).

[27] W. Ren et al., "Simultaneous excitation of two noninteracting atoms with time-frequency correlated photon pairs in a superconducting circuit", Physical Review Letters **125**, 133601 (2020).

[28] M. F. Gely et al., "QuCAT: quantum circuit analyzer tool in python", New Journal of Physics **22**, 013025 (2020).

[29] M. Pechal, "Microwave photonics in superconducting circuits", PhD thesis (ETH Zurich, 2016).

[30] *LD dilution refrigerator measurement system*, Bluefors, `https://bluefors.com/products/ld-dilution-refrigerator/`.

[31] M. Naghiloo, "Introduction to experimental quantum measurement with superconducting qubits", arXiv:1904.09291 [quant-ph] (2019).

[32] M. Scigliuzzo et al., "Primary thermometry of propagating microwaves in the quantum regime", Physical Review X **10**, 041054 (2020).

[33] X. Y. Jin et al., "Thermal and residual excited-state population in a 3d transmon qubit", Physical Review Letters **114**, 240501 (2015).

DEPARTMENT OF SOME SUBJECT OR TECHNOLOGY
CHALMERS UNIVERSITY OF TECHNOLOGY
Gothenburg, Sweden
www.chalmers.se

CHALMERS
UNIVERSITY OF TECHNOLOGY